

Reactive nitrogen in and around the northeastern and Mid-Atlantic US: sources, sinks, and connections with ozone

Min Huang^{1,2}, Gregory R. Carmichael³, Kevin W. Bowman⁴, Isabelle De Smedt⁵, Andreas Colliander⁴, Michael H. Cosh⁶, Sujay V. Kumar¹, Alex B. Guenther⁷, Scott J. Janz¹, Ryan M. Stauffer¹, Anne M. Thompson¹, Niko M. Fedkin¹, Robert J. Swap¹, John D. Bolten¹, Alicia T. Joseph¹

¹Earth Sciences Division, NASA Goddard Space Flight Center, Greenbelt, MD 20771, USA

²Earth System Science Interdisciplinary Center, University of Maryland, College Park, MD 20740, USA

³College of Engineering, University of Iowa, Iowa City, IA 52242, USA

⁴Jet Propulsion Laboratory, California Institute of Technology, Pasadena, CA 91109, USA

10 ⁵Royal Belgian Institute for Space Aeronomy, 1180 Brussels, Belgium

⁶Hydrology and Remote Sensing Laboratory, US Department of Agriculture, Beltsville, MD 20705, USA

⁷Department of Earth System Science, University of California at Irvine, Irvine, CA 92697, USA

Correspondence to: Min Huang (minhuang@umd.edu)

Abstract. This study describes an application of a regional Earth system model (NASA-Unified Weather Research and Forecasting with online chemistry) with updated parameterizations for selected land-atmosphere exchange processes and multi-platform, multidisciplinary observations. First, we estimate reactive nitrogen (Nr = oxidized NO_y + reduced NH_x) emissions from anthropogenic and natural sources, nitrogen dioxide (NO₂) column densities and surface concentrations, total and speciated Nr dry or/and wet deposition fluxes during 2018–2023 over the northeastern and Mid-Atlantic US, most of which belong to nitrogen oxides-limited or transitional chemical regimes. The estimated multi-year Nr concentrations and deposition fluxes are then related to ozone (O₃), in terms of their spatiotemporal variability and key drivers as well as possible ecosystem impacts. Finally, through three sets of case studies, we identify and discuss about 1) the capability of land data assimilation (DA) to reduce the uncertainty in modeled land surface states at daily-to-interannual timescales that can propagate into atmospheric chemistry fields; 2) the impacts of irrigation on land surface and atmospheric fields as well as pollutants' ecosystem uptake and impacts; and 3) the impacts of transboundary air pollution during selected extreme events on pollutants' budgets and ecosystem impacts. With the updated model parameterizations and anthropogenic emission inputs, the eastern US surface O₃ modeled by this tool persistently agrees better with observations (i.e., with root-mean-square errors staying within 4–7 ppbv for the individual years' May-June-July) than many of those in literature where model errors are often tens of ppbv. The model-based correlation between daytime surface O₃ and early afternoon NO₂ columns, which shows a dependency on column HCHO/NO₂ ratios, is higher in 2020 ($r=0.62$) than in other years during 2018–2023 ($r=0.47$ – 0.56). The O₃ vegetative uptake overall dropped by ~10% from 2018 to 2023, displaying clearer downward temporal changes than the total Nr deposition due to the declining NO_y emission and deposition fluxes competing with the increasing NH_x fluxes. It is highlighted that, temporal variability of Nr and O₃ concentrations and fluxes on subregional-to-local scales respond to hydrological variability that can be influenced by precipitation and controllable human activities such

as irrigation. Deposition processes and biogenic emissions that are highly sensitive to interconnected environmental and plants' physiological conditions, as well as extra-regional sources (e.g., O₃-rich stratospheric air and dense wildfire plumes from upwind regions), have been playing increasingly important roles in controlling pollutants' budgets in this area as local emissions go down owing to effective emission regulations and COVID lockdowns. To better inform the design of mitigation and adaptation strategies, it is recommended to continue evaluating and improving the model parameterizations and inputs relevant to these processes in seamlessly coupled multiscale Earth system models using laboratory and field experiments in combination with satellite DA which would in turn benefit remote sensing communities.

1 Background, motivation, and goals

Nitrogen oxides (NO_x) are an important group of ozone (O₃) precursor and destroyer, and ground-level O₃ is a US Environmental Protection Agency (EPA)-regulated criteria air pollutant. NO_x consists of nitric oxide (NO) and nitrogen dioxide (NO₂), the latter of which is another US EPA-regulated criteria air pollutant that has the highest exposure disparities (Liu et al., 2021). Emitted from various anthropogenic (anth) and natural sources, NO_x is readily transformable to/from other forms of reactive nitrogen (Nr = oxidized NO_y + reduced NH_x) species, such as ammonia (NH₃), peroxyacetyl nitrate (PAN) and nitric acid (HNO₃). Some of these chemical reactions also contribute to fine particulate matter pollution, which is connected with O₃ via aerosol radiative effects and heterogeneous chemistry (Seinfeld and Pandis, 2016; Monks et al., 2021). Many previous studies have demonstrated that NO_x emissions and concentrations play more crucial roles than volatile organic compounds (VOCs) in regulating the magnitude and spatiotemporal variability of O₃ (e.g., Duncan et al., 2010; Jin et al., 2017; Koplitz et al., 2022; Souri et al., 2023) as well as aerosols (Carlton et al., 2010; Holt et al., 2015) in much of the northeastern and Mid-Atlantic states, the most populous US region where the land surface is highly heterogeneous and hydroclimatic extremes and exceedances of the US National Ambient Air Quality Standards occur from time to time (US Global Change Research Program, 2023; US EPA, 2023). An improved understanding of the sources, sinks, and distributions of NO_x and Nr as well as how these have been and will be changing through time is beneficial for interpreting O₃ air pollution levels and their spatiotemporal variability in this area. The removals of Nr, O₃, and other chemicals involved in their life cycles from the atmosphere through wet or/and dry deposition closely interact with multiple other interconnected environmental stressors (e.g., temperature, humidity, precipitation, soil moisture, SM, and carbon dioxide, CO₂) and plants' physiological conditions. Together, they can cause intertwined and cascading effects on the diverse terrestrial and aquatic ecosystems (e.g., United Nations Economic Commission for Europe, 1999; Galloway et al., 2003, 2004; Felzer et al., 2009; Simpson et al., 2014; Lombardozzi et al., 2015; Mills et al., 2018; Walker et al., 2019; Clifton et al., 2020; Emberson, 2020) in this area. Due to effective environmental regulations and unusual situations such as COVID lockdowns, anth emissions continue to decrease there. For studies on Nr and O₃, attention should also be given to quantifying the impacts of multiple climatic factors as well as nonlocal air pollution sources such as those imported from upwind US regions, Canada, and the

65 stratosphere, which are partially controlled by the Bermuda High and other pressure systems (e.g., Colarco et al., 2004; Zhu et al., 2013; Ott et al., 2016; Rogers et al., 2020).

Previous global and regional modeling studies have shown that reproducing the observed warm-season Nr and surface O₃ levels in the US East is challenging (e.g., Fiore et al., 2009; Chai et al., 2007, 2013; Lapina et al., 2014; Huang et al., 2017a; 70 Lin et al., 2017). The estimated background O₃ therein, as well as the importance of its individual contributors, varies substantially among models. Often, the large model-observation mismatches in surface O₃ of up to tens of ppbv were not well explained or attributed mainly to the models' uncertain/outdated anth emission inputs. Some of these studies implemented advanced chemical data assimilation (DA) methods to reduce the errors in their predicted surface O₃ states by ~50% (Chai et al., 2007). They did not improve the mechanistic representations of O₃ related processes, which are of higher 75 policy-relevance and would lengthen the impacts of chemical DA since the model initializations/analysis times. The large uncertainty in model results limits our capability of understanding air quality over these regions and evaluating potential strategies to mitigate the air pollution impacts. High-resolution Earth system modeling with proper model parameterizations, up-to-date inputs, and comprehensive, process-based analysis aided by cross-disciplinary observations can help elucidate the various factors controlling Nr and O₃ (Fig. 1a) to better assist with assessing their environmental impacts from past to future.

80

This study is designed to support the International Global Atmospheric Chemistry-Tropospheric Ozone Assessment Report (TOAR) Phase II activity, which aims to further examine the distributions, temporal changes, and impacts of O₃ and its key precursors. A regional Earth system model is applied with updated parameterizations for selected land-atmosphere exchange processes (Section 2.1), running over the Northeast and Mid-Atlantic states for multiple years at 10 km horizontal resolution 85 that is considered to be able to better capture NO_x lifetime and budgets than coarser resolution systems (Li et al., 2023). The model is used together with multiplatform, multidisciplinary observations (Section 2.2) and a range of analysis methods (e.g., model evaluation and diagnosis, formal DA, and sensitivity simulations, Section 2.3) to help achieve the following specific goals: 1) to estimate Nr emissions from various anth and natural (e.g., soil NO and nitrous acid, HONO) sources, NO₂ surface concentrations and column densities, total and speciated Nr dry or/and wet deposition fluxes during 2018–2023, 90 with discussions on key anth and environmental/climatic drivers of their spatiotemporal variability during this period (Section 3.1); 2) to relate Nr and O₃ concentrations as well as their deposition fluxes during 2018–2023, in terms of spatiotemporal variability, reactions to environmental and biophysical stresses, and potential ecosystem impacts (Section 3.2); and 3) through three sets of case studies (Section 3.3), to discuss in detail about land-atmosphere exchange processes which have been understudied topics. Specifically, we demonstrate the capability of land DA to reduce the uncertainty in the 95 modeled land surface states, land-atmosphere exchange processes and atmospheric states at daily-to-interannual timescales; the impacts of controllable human activities such as irrigation on land surface and atmospheric fields and pollutants' ecosystem uptake; and the impacts of transboundary air pollution during selected extreme events on air pollutants' budgets

and ecosystem impacts. These case studies also help identify sources of model uncertainty before we draw conclusions and outline future directions for further advancements in related areas in Section 4.

100 2 Methods

2.1 Coupled modeling system and the baseline simulation

On a 10 km, 63 vertical layer Lambert conformal grid (Fig. 1b–c) from the subsurface to ~100 hPa, the NASA-Unified Weather Research and Forecasting model with online chemistry (WRF-Chem) simulations were conducted over the Northeast and Mid-Atlantic states for 2018–2023 growing seasons starting from 25 April of each year. The analysis of the baseline simulation was focused on May–June–July (MJJ) of 2018–2020, 2022, and 2023. MJJ falls within the plant growing and O₃ seasons when atmospheric Nr and O₃ most actively interact with ecosystems (Li et al., 2015; Clifton et al., 2020). Year of 2021 is not an emphasis in this paper partly due to the lack of reliable information to represent the COVID impacts on anth emissions for that year. The four-layer Noah-Multiparameterization (MP, Niu et al., 2011) land surface model (LSM) version 3.6 within the NASA Land Information System served as the land component of this modeling system, running with a sprinkler irrigation and the Community Land Model type of SM factor controlling stomatal resistance (i.e., β factor) schemes. Noah-MP was forced by the North American Land Data Assimilation System Phase 2 forcing data during the long-term (since 2000) offline spin-up. Noah-MP’s CO₂ forcings for 2018, 2019, 2020, 2022, 2023’s warm seasons were set to 410, 412, 415, 420, and 423 ppmv, respectively, based on measurements at the Mauna Loa Observatory and its nearby Maunakea Observatories for part of 2023 (https://gml.noaa.gov/webdata/ccgg/trends/co2/co2_mm_mlo.txt, last access: 12 January 2024). This advanced Noah-MP’s default setup in terms of appropriately representing the global CO₂ growth rates of 2–3 ppmv year⁻¹ for recent years (https://gml.noaa.gov/ccgg/trends/gl_gr.html, last access: 12 July 2024). Ignoring the spatial and (intra)seasonal variability in CO₂ of up to tens of ppmv over the study region (Karion et al., 2020) may have introduced only small uncertainty in photosynthesis and deposition modeling according to independent model sensitivity analysis in which CO₂ forcings were perturbed (e.g., Sun et al., 2022). The land use/land cover (LULC) and soil type inputs of Noah-MP were based on the 20-category International Geosphere-Biosphere Programme-modified Moderate Resolution Imaging Spectroradiometer (MODIS, Fig. 1b) and the 16-category State Soil Geographic (Fig. S1) datasets, respectively. Crop-type and irrigation map/fraction information required by the irrigation scheme came from Monfreda et al. (2008) and Salmon et al. (2015), respectively, the latter of which (Fig. 1c) incorporated MODIS information.

125 Major atmospheric and land model physics as well as chemistry schemes were configured in similar ways to those in Huang et al. (2022). The photosynthesis-based dry deposition approach recommended in Huang et al. (2022) and a number of other previous dry deposition studies cited therein was applied to most gaseous species. No change was made to sulfur dioxide dry deposition approach (Erisman et al., 1994) for this study. The modeled wet deposition fluxes were also evaluated and discussed in this work. In replacement of the metric-based approach in Huang et al. (2022), O₃ vegetative impacts were

130 dynamically modeled by applying two separate factors to photosynthesis and stomatal conductance rates (Lombardozi et al., 2015) that are calculated in Noah-MP. These factors are land cover-dependent functions of O₃ uptake cumulated during growing season when leaf area index (LAI) exceeds 0.5. To account for the ability of plants to detoxify O₃, O₃ fluxes were only accumulated when they exceeded a threshold of 1.0 nmol O₃ m⁻² s⁻¹. As demonstrated in previous offline (Lombardozi et al., 2015) and online (Li et al., 2016; Sadiq et al., 2017) modeling studies, dynamically modeling O₃ vegetative impacts
135 could help quantify the perturbations of O₃ to a variety of hydrological, ecological, and weather variables. Online-calculated biogenic emissions of O₃ precursors such as VOCs and Nr species in the simulations were adjusted to be more sensitive to multiple environmental stresses. Specifically, a drought adjusting factor γ_d was introduced in the Model of Emissions of Gases and Aerosols from Nature (MEGAN) biogenic isoprene emission calculations following the suggestions by Jiang et al. (2018), which depends on the β factor and the maximum carboxylation rate. The plant function type information needed for
140 MEGAN was converted from the annual European Space Agency Climate Change Initiative (ESA CCI) land cover product for 2018–2020, and the 2020 data from this product were also used for the years afterwards. The Noah-MP modeled LAI_v (i.e., LAI/Green Vegetation Fraction) feeds into MEGAN calculations. Soil emissions of NO were estimated largely based on the mechanism recommended by Hudman et al. (2012) and Simpson and Darras (2021), i.e., for dry and wet soils that are determined by a SM index (i.e., a function of SM, soil wilting point and field capacity), different sets of biome-based
145 emission coefficients (Steinkamp and Lawrence, 2011) and the standing Nr pool plus nitrogen input from deposition being adjusted by water-filled pore space θ (i.e., SM divided by porosity), soil temperature (Wang et al., 2021), and canopy reduction factor. The pulsing effects, which are small for this study area/season, were accounted for. Soil HONO emissions were also calculated online, scaled from soil NO emissions using biome-dependent factors specified in Table A1 of Rasool et al. (2019) that were partly adapted from Oswald et al. (2013). Nitrogen input from fertilizer was not included in the soil
150 emissions calculations to avoid double counting with agricultural emissions from the anth emission input to be introduced below. Oceanic natural NH₃ emissions were not included, which were estimated to have negligible impacts on Nr overland (Paulot et al., 2013). Lightning emissions were also calculated online and vertically distributed adopting the setup described in Huang et al. (2021) which was based on cloud-top-height-based parameterizations (Wong et al., 2013) and climatological intra-cloud to cloud-to-ground flash ratios. A passive lightning NO_x tracer was again implemented, that experienced
155 atmospheric transport but not chemical reactions. Aerosol direct, semidirect and indirect radiative effects were enabled.

Emissions from various anth source sectors came from the Copernicus Atmosphere Monitoring Service (CAMS) global inventory version 5.3, available at 0.1°×0.1° horizontal resolution with monthly and year-by-year variability. To account for COVID impacts, for 2020, grid- and sector-dependent factors (Dombia et al., 2021) were applied to adjust the emissions.
160 This CAMS inventory for the years after 2015 was developed by extrapolating the Emissions Database for Global Atmospheric Research version 5 based on the Community Emissions Data System version 2 trends and including emissions from ships as well as monthly variability that were estimated separately (Granier et al., 2019; Soulie et al., 2024). It's noted in Elguindi et al. (2020) and references therein that NO_x emissions for recent decades from an earlier version of CAMS

inventory do not notably differ from other bottom-up inventories over the US where more detailed information for emission
165 inventory developments are available. In contrast, top-down estimates diverge significantly due to uncertainty in the used
satellite NO₂ retrievals as well as the model representations of various atmospheric processes many of which are scale-
dependent. A clear understanding of the impact of background NO_x sources, including natural emissions, on constraining
NO_x emissions with satellite NO₂ data is urgently needed. The 0.1°×0.1°, version 2.6r1 of the Quick Fire Emissions Dataset
(QFED, Darmenov and da Silva, 2015), developed with the fire radiative power approach, was applied with plume rise
170 (Grell et al., 2011). QFED NO_x emissions over North America during 2012–2019 are in comparable magnitudes with other
widely-used fire emission datasets such as the Fire INventory from NCAR (FINN) while its NH₃ emissions are higher than
the estimates from other products (Wiedinmyer et al., 2023). Figure 2 presents the total anth and biomass burning (fire) NO_x
and NH₃ emissions averaged for each year's MJJ. Anth NO_x emissions are shown to decrease due to effective emission
controls (i.e., a -16.3% overall change from 2018 to 2023), except for slight increases along a few shipping lanes. They are
175 anomalously low in 2020 (~23.8% lower than 2018) largely due to reduced human activities during the COVID lockdowns.
The temporal changes in non-methane (NM) VOC emissions are relatively smaller, with the domain-mean in 2023 only ~6%
lower than in 2018. The total anth NH₃ emissions were growing in many places, most evidently over croplands as a result of
the rising agricultural soil and livestock emissions. The QFED-based fire NO_x and NH₃ emissions were generally increasing,
reaching their highest in 2023.

180

Daily reinitialized atmospheric initial conditions (ICs) and boundary conditions (BCs) were downscaled from the 3-hourly,
32 km North American Regional Reanalysis (NARR) dataset, which overall well represents the observed daily variability in
apparent temperature for the eastern US (e.g., Ibebuchi et al., 2024). Huang et al. (2017b) showed that, initializing WRF with
the North American Mesoscale Forecast System (6-hourly, 12 km)'s atmospheric fields instead of NARR's did not result in
185 significant changes in WRF-simulated surface air temperature fields over the southeastern US. A set of the 6-hourly
Community Atmosphere Model with Chemistry (CAM-Chem, for 2018–2020, 0.9°×1.25°/56 vertical levels) and Whole
Atmosphere Community Climate Model (WACCM, beyond 2020, 0.9°×1.25°/88 vertical levels) simulations that also
ingested QFED fire information served as the chemical BCs of the WRF-Chem baseline simulation because of its higher
completeness of chemical species, and for WACCM, its availability for very recent years compared to chemical reanalysis
190 products which are likely to be more accurate. The chemical BC models' stratospheric O₃ tracer fields also supported our
multi-year analysis and a case study (Section 3.3.3). From 2018 to 2023, the lower free tropospheric O₃ in MJJ first rose by
up to 4 ppbv, and then dipped down by up to 4–6 ppbv before rising again (Fig. 3a). The interannual variability in lower free
tropospheric O₃ and its precursors upwind of the eastern US, as well as the synoptic wind fields that shifted from westerly in
2018–2022 to northwesterly in 2023 (Fig. 3c), play critical roles in controlling the modeled large-scale O₃ patterns and their
195 temporal changes. Ozone transport from the stratosphere more strongly influenced the lower free tropospheric O₃ over the
southern part of our domain in 2023 than in 2018 by up to 4 ppbv (Fig. 3a–b). Although the stratospheric air influences on

surface O₃ were diluted to no more than a few ppbv (Fig. S2), the challenges regional models experience in reproducing their magnitudes and interannual variability may introduce uncertainty to the estimated surface O₃ changes.

2.2 Observations

200 2.2.1 Chemical observations from satellites, aircraft, and ozonesondes

The TROPospheric Monitoring Instrument (TROPOMI) on board the Copernicus Sentinel-5 Precursor satellite launched in 2017 provides trace gas and aerosol measurements at daily global coverage since April 2018, with ascending node ~13:30 local time overpasses. It has much finer resolutions (i.e., 3.5×5.5 km² at nadir since August 2019, and 3.5×7 km² before then), a wider spectral range and higher signal-to-noise ratio per ground pixel than its predecessors. TROPOMI data have demonstrated their robustness in studying air pollution from numerous source sectors (e.g., land and water traffic, power plants, oil, gas and other industries, biogenic and fire) in greater detail (e.g., Georgoulias et al., 2020; van der Velde et al., 2021; Griffin et al., 2021; Goldberg et al., 2021; Dix et al., 2022). In this study, the gridded (0.02°×0.02°) monthly and daily level 2 TROPOMI tropospheric vertical column NO₂ data were analyzed together with WRF-Chem fields to help understand the temporal changes in column NO₂. The gridded (0.05°×0.05°) monthly TROPOMI formaldehyde (HCHO) tropospheric vertical columns (De Smedt et al., 2021) were also used to calculate HCHO/NO₂ ratios to help determine O₃ chemical regimes over the study area. The TROPOMI-based HCHO/NO₂ ratios were supplemented by those derived from the gridded (1 km×1 km) NO₂ and HCHO data collected on selected days of 2018 over New York City and the Long Island Sound by two similar airborne instruments (Judd et al., 2020) Geostationary Trace gas and Aerosol Sensor Optimization (GeoTASO) and GEO-CAPE Airborne Simulator (GCAS).

215

Additionally, to help identify and attribute air pollutants during highly polluted events in 2023 (Section 3.3.3), the Joint Polar Satellite System-1 Cross-track Infrared Sounder (JPSS-1/CrIS, with descending/ascending nodes of ~1:30/13:30 local time) O₃, carbon monoxide (CO), and PAN level 2 daily summary data provided by the Tropospheric Ozone and Precursors from Earth System Sounding project, were analyzed. The analysis of these extreme events was also supported by eight ozonesondes launched from the Virginia Commonwealth University Rice Rivers Center (RRC, 37.33197°N, 77.20842°W) during the inaugural edition of NASA Student Airborne Research Program (SARP)-East campaign in summer 2023 along with model results and ground-based observations (Section 2.2.3).

225

2.2.2 Satellite SM and precipitation products

To characterize drought conditions and their temporal variability, which interact with atmospheric chemistry, NASA's L-band Soil Moisture Active Passive (SMAP) 9 km enhanced surface (first 5 cm belowground) SM (SSM) data version 5 were utilized, as well as the version 7 of daily precipitation data from the NASA-JAXA Global Precipitation Measurement (GPM) produced at 0.1°×0.1° resolution using the Integrated Multi-satellitE Retrievals for GPM-Final run algorithm. Despite the different sampling strategies and retrieval algorithms of SMAP and GPM, interannual variability in the drought conditions

230 indicated by these SSM and precipitation data are qualitatively consistent (Fig. 4), which are also consistent with information
from independent sources such as the North American Drought Monitor (<https://droughtmonitor.unl.edu/NADM>, last access:
12 July 2024; see Table S1 and Fig. S3 for further analysis and discussions). In addition to rainfall, irrigation water and other
elements relevant to water and energy balances can also impact the variability in SSM which has feedback to the regional
precipitation patterns. The wide range of the SMAP SSM from <0.2 to $>0.5 \text{ m}^3 \text{ m}^{-3}$ and its interannual differences which
235 often exceed $0.1 \text{ m}^3 \text{ m}^{-3}$, indicate the diverse SM regimes (i.e., dry, transitional, and wet) and therefore spatially and
temporally varying land-atmosphere coupling strengths (Seneviratne et al., 2010, and references therein). The varying SSM-
temperature coupling strengths were determined based on WRF-Chem results, with support of the $0.25^\circ \times 0.25^\circ$ European
Centre for Medium-Range Weather Forecasts Reanalysis version 5 (ERA5) surface air temperature field. In a case study
(Section 3.3.1), SMAP SSM data were assimilated into the Noah-MP LSM to improve the land ICs of WRF-Chem, and
240 further, the modeled weather and atmospheric chemistry fields.

2.2.3 Ground-based observations

Hourly surface ultraviolet absorbance O_3 observations from the US EPA's Air Quality System (AQS, a major source of the
TOAR database, last update in August 2024) were used to support the quantification of O_3 temporal variability and model
245 evaluation. The AQS NO_2 observations, which have poorer spatial coverage than their O_3 data, were also examined to help
qualitatively understand surface NO_2 variability. These AQS NO_2 measurements made using the chemiluminescence
detection with catalytic conversion are known to be positively biased by up to 50% due to NO_z (NO_y - NO_x) interferences
(e.g., Dunlea et al., 2007). Speciated aerosol measurements offered by the Clean Air Status and Trends Network
(CASTNET) and AQS, CASTNET HNO_3 , the National Atmospheric Deposition Program (NADP)/Ammonia Monitoring
250 Network (AMoN) NH_3 observations, as well as the NADP/National Trends Network (NTN) wet deposition fluxes and
precipitation data, were used to infer or directly evaluate WRF-Chem's deposition performance. Deposition datasets from
other studies, some of which integrated surface or/and satellite observations with other models (e.g., Schwede and Lear,
2014; Fu et al., 2022; Rubin et al., 2023), will be referred to in the discussions.

255 Additional datasets for selected time periods were used in DA case studies to help interpret and validate the model results
(Section 3.3.1). These include gauge-based precipitation data and SSM measured using HydraProbe sensors at Harvard
Forest, Massachusetts (42.53523°N , 72.17393°W) and a US Climate Reference Network (CRN) site in Millbrook, New
York (41.786°N , 73.74°W) during the July 2022 SMAP validation experiment (SMAPVEX22); and surface air temperature
observations in July 2018 and 2022 from the National Centers for Environmental Prediction (NCEP) Global Surface
260 Observational Weather Data product.

2.3 Case studies and sensitivity simulations

Temporal variability of Nr and O₃ concentrations and fluxes at subregional-to-local scale are partially driven by hydrological variability which can be influenced by both precipitation and human activities such as irrigation. Two sets of modeling and DA case studies (Sections 2.3.1 and 2.3.2) were conducted to show that the modeled land surface states, such as SM, can be improved via land DA and/or updating the model's irrigation schemes, which further impacts the modeled land-atmosphere exchange processes and atmospheric fields.

2.3.1 Effects of SM DA on modeled NO₂ and O₃

For this case study, SMAP morning-time (~6 am local time) SSM data were bias-corrected via matching the means and standard deviations of SMAP and Noah-MP SSM monthly climatology. The bias-corrected data were then assimilated into the Noah-MP LSM using a 40-member ensemble Kalman filter approach to adjust WRF-Chem's land ICs during July 2018 and July 2022. Meteorological forcing (precipitation, short- and longwave radiation) and state (Noah-MP SM) perturbation attributes were set up largely based on Kumar et al. (2009) recommendations for the Noah LSM, and the input observation error standard deviation was set to be 0.04 m³ m⁻³ according to the SMAP data quality requirement. Through this experiment we evaluate whether and to what extent can satellite SM DA improve the day-to-day (i.e., before and after a precipitating event during the SMAPVEX22 campaign when in situ SSM data were also collected near the SMAP morning overpassing times) and interannual variability (i.e., July 2018 and July 2022) of Noah-MP SM, even in dense vegetation regions such as the eastern US where satellite SM retrieval is generally more challenging. How the adjustments to Noah-MP land surface states by DA impacted the modeled atmospheric fields was also quantified.

2.3.2 Irrigation impacts on O₃ vegetation uptake and Nr deposition

Using flux-based O₃ metrics derived from model outputs, recent studies (Mills et al., 2018; Huang et al., 2022) estimated that the negative impacts of ground-level O₃ on crop yields are particularly large in humid irrigated and rainfed agricultural lands, where the plants' stomatal uptake of O₃ is significant. The global-scale coarse-resolution analysis for 2010–2012 by Mills et al. (2018), which was based on O₃-flux metrics, also estimated that irrigation promotes the O₃ impacts on wheat production by up to ~10%. To dynamically evaluate in detail the irrigation impacts on land surface and atmospheric fields as well as the estimated O₃ and Nr ecosystem impacts across our study area for recent years, WRF-Chem simulations were conducted with three sets of irrigation configurations, defined as (a, b, c) below, and for each of these three scenarios, two simulations were conducted with and without O₃ vegetation impacts:

- a) Full irrigation (baseline): Sprinkler irrigation occurs in the morning when rootzone SM drops below 50% of field capacity;
- 290 b) Reduced irrigation: Sprinkler irrigation occurs in the morning when rootzone SM drops below 25% of field capacity, and the estimated irrigation water usage for this scenario is ~1/6 of the full-irrigation scenario for irrigated areas south of ~37°N in our domain;
- and c) Irrigation option was completely disabled.

This sensitivity analysis is focused on 21–30 June 2022, when irrigated fields in the Carolinas that grow mostly O₃-sensitive crops were under stress according to the Vegetation Drought Response Index produced by the National Drought Mitigation Center (Fig. S4). This region also encompasses Nr deposition hotspots that have been experiencing critical load (CL) exceedances (i.e., the amount of Nr deposition exceeds the CL threshold, the point above which deposition could harm sensitive ecosystems). For this period, irrigation water consumption under the full-irrigation scenario may be higher than normal, and the estimated surface fluxes under reduced- and no-irrigation scenarios may be particularly smaller than usual and more strongly constrained by SM.

2.3.3 Impacts of transboundary pollution on weather, air quality and ecosystems

The Northeast and Mid-Atlantic US air quality is regularly affected by pollutants emitted or/and formed in upwind US states. Actions have been taken to tackle cross-state air pollution such as using the Cross-State Air Pollution Rule framework (<https://www.epa.gov/Cross-State-Air-Pollution/overview-cross-state-air-pollution-rule-csapr>, last access: 12 January 2024). However, with the US EPA’s “Good Neighbor Plan” being put on hold by the Supreme Court (<https://www.epa.gov/Cross-State-Air-Pollution/good-neighbor-plan-2015-ozone-naaqs>, last access: 12 July 2024), downwind US states may continue to face difficulties in complying with the 2015 O₃ National Ambient Air Quality Standards due to the upwind states’ pollution impacts. Periodically, distant sources including Canadian wildfires and O₃-rich stratospheric air also travel to the northeastern and Atlantic states. Satellite and in situ observations are powerful in detecting such episodic events that occur more frequently in recent years, assisting with early warnings and early actions. To help quantify the impacts of such extreme events, as well as other upwind air pollution sources, on weather, air quality and ecosystems during 13–16 June 2023, two WRF-Chem sensitivity simulations were conducted and analyzed together with the baseline simulation and multiplatform observations. Clean chemical BCs were applied in one of these sensitivity simulations, and WACCM running with the FINN fire emission input served as the chemical BCs of the other WRF-Chem sensitivity simulation named “Sen”. Fire emission is identified as one of the most important configurations in global wildfire modeling (e.g., Veira et al., 2015).

3 Results and discussions

3.1 Nr emissions, concentrations, and deposition fluxes during 2018–2023

The modeled soil NO and HONO emissions vary strongly with SM as well as soil temperature that can be impacted by SM. Even without land DA the model fairly well reproduced the large-scale spatial gradients and interannual variability of soil wetness (Figs. 4a and S5). Soil emissions exhibit notable monthly variations, with multi-year June- and July-mean values ~11% and ~59% higher than the May-mean, respectively, associated with overall warmer and drier conditions. These monthly variations, together with the ~8% and ~18% multiyear June-May and July-May mean differences in anth+fire emissions as well as modeled surface and column NO₂ fields, help interpret the higher TROPOMI and AQS NO₂ on warmer months over many rural areas, especially those near high-temperature agricultural regions (Fig. S6), a point Goldberg et al. (2021) also highlighted. The maxima and minima of MJJ soil emissions are shown in 2020 and 2018, respectively, and the

interannual variability of soil emissions roughly anti-correlates with that of SM, with correlation coefficient r ranging from -0.63 to -0.40 ($p < 0.01$; Fig. 5a,c). For most years, the estimated MJJ-mean soil NO and HONO emissions are particularly high in warm and/or dry areas including parts of the Carolinas, Virginia, New York, Michigan, and Canada's Ontario, where their contributions to the total soil+anth+fire NO_y emissions persistently exceeded 30% (Fig. 5a–b). Based on a global atmospheric chemistry model with a similar soil emission scheme, previous estimates of the soil NO emission contributions to column NO₂ for this area were minor compared to other US regions in 2005 (i.e., <15% uniformly, Vinken et al., 2014), when anth NO_x emissions were >25% higher than in 2018 according to the CAMS inventory and other estimates. Owing to the overall declining US anth emissions and the changing climate, soil emissions play an increasingly important role in controlling Nr, and further, O₃ air quality, in this area. Accordingly, the needs to properly parameterize soil emissions and accurately model soil environments (e.g., SM, soil temperature, pH) have been growing stronger which could greatly benefit from laboratory and field experiments.

Despite the increasing anth NH₃ and fire Nr emission trends (Section 2.1) and the abovementioned interannual variability in soil NO and HONO emissions, the total Nr emissions as well as surface NO_y emissions that contributed to >50% of the total Nr emissions show decreasing year-to-year changes during 2018–2023 except for the dip in 2020 that is mainly attributable to the COVID lockdowns (Fig. 6a). Closely linked to such temporal changes in NO_y emissions, that in many areas overwhelm the effects of slower NO₂ and NO_y dry deposition (Fig. S7 and later discussions), the modeled column and surface NO₂ both display downward changes since 2018, with their lowest values occurring in 2020 (Figs. 6b and 7). From 2018 to 2023, on average, column and surface NO₂ dropped by 15–20%. Impacted by the decreasing NO₂, HCHO columns overall demonstrate a few percent slower year-to-year changes than NO₂ (Fig. S8), in large part because of less significant NMVOC emission changes (Section 2.1). Impacted mostly by shipping and lightning emissions as well as North American pollution outflows, the amount of NO₂ above the ocean is lower than overland. Early afternoon (19 UTC, local standard time +5 or +6, near TROPOMI overpassing times) surface and column NO₂ are ~44% and ~29% lower than their daytime averages (13–24 UTC, roughly the sampling times of geostationary missions such as the Tropospheric Emissions: Monitoring of Pollution, TEMPO, and the anticipated Geostationary Extended Observations). The stronger subdaily variability in surface NO₂ than in column NO₂ reflects the impacts of photochemistry and evolution of planetary boundary layer on the rapidly changing vertical distributions of chemicals throughout the daytime which have also been demonstrated in Huang et al. (2017b) and other studies with aircraft observations. Dependent strongly on convection, lightning NO emissions show high variations from year to year in terms of locations and magnitudes, having larger impacts on free-tropospheric and column-average NO₂ than surface NO₂ (Fig. S9).

The column NO₂ spatiotemporal variability based on WRF-Chem and TROPOMI greatly resemble one another (Fig. 7a–b), and larger model-TROPOMI discrepancies are seen over the areas possibly influenced by lightning NO emissions and transboundary pollution where both model and retrieval errors may be large. The interannual variations in such pollutant

sources aloft may also explain the different interannual variability in surface and column NO₂ for some locations and years. AQS NO₂ data, although sparsely distributed and positively biased, qualitatively confirmed the model-suggested year-to-year changes in surface NO₂ (Fig. S10).

365 Drought conditions, as well as the opposite directions of NO_y and NH₃ emission and concentration changes, helped shape the interannual variability in the total Nr deposition fluxes (Fig. 8a). Overland, the modeled Nr wet deposition fluxes often contributed to nearly or lower than 30% of the total Nr deposition. These contributions are smaller than earlier estimates for this area (e.g., <60% in Tan et al., 2018, where wet deposition based on 11 global models was overestimated), due in part to WRF-Chem wet deposition being underestimated referring to the NADP/NTN measurements (Table S2 and Fig. S11). This
370 underestimation in wet deposition can be attributed to known limitations in the WRF-Chem wet deposition scheme (Ryu and Min, 2022; Yao et al., 2023). The underestimated model precipitation rates and inaccurate model precipitation patterns on event-to-seasonal scales (Figs. 4b, S5, and S11; Section 3.3.1 case study), as well as observation representation errors, also have caused the negative biases in wet deposition fluxes and the positive biases in aerosol concentrations especially for NH₄ and NO₃ (Figs. S11–S14). Such precipitation biases in WRF have also been reported in previous studies, and they can
375 indirectly impact dry deposition modeling.

Dry NO_y deposition fluxes decreased evidently (i.e., by 5–16% overall and >50% in some populated areas) whereas NH_x dry deposition fluxes show up to ±3% of overall interannual variability and rose by >20% over certain agricultural lands (Fig. S15) where NH₃ emissions have been climbing up. Due to not applying a bi-directional approach (Zhang et al., 2010; Massad et al., 2010; Pleim et al., 2019), these NH₃ fluxes may be overestimated over source regions by a few percent (Zhu et al., 2015; Liu et al., 2020a), contributing to the model’s minor negative NH₃ biases relative to the NADP/AMoN data (Table S2 and Fig. S13). Nevertheless, the contrasting directions of change in NO_y and NH_x deposition fluxes as well as the importance of NH_x deposition in total deposition corroborate results from other studies for earlier periods (e.g., Schwede and Lear, 2014; Li et al., 2015; Jia et al., 2016; Geddes and Martin, 2017; Liu et al., 2020b, and references therein). With several
385 percent of interannual differences in flux partitioning (Fig. 8b–c), in all years’ MJJ, HNO₃ and NH₃ contributions (>35%) dominated in the Nr dry deposition fluxes. NO dry deposition is negligible due to extremely high surface resistance and in figures is combined with NO₂ into NO_x fluxes, that contribute to 12–15% of Nr dry deposition fluxes. Unlike most other species, surface resistance of HNO₃ is nearly zero, whose dry deposition variability is therefore driven dominantly by aerodynamic resistance and quasi-laminar sublayer resistance and responds differently to drought conditions than the other
390 Nr species and O₃ (Section 3.2). The modeled HNO₃ daytime dry deposition velocities over most forested areas fall within 4–8 cm s⁻¹, close to the measurements reported in literature for similar land cover types in the eastern US (e.g., Nguyen et al., 2015). These are ~a factor of 10 higher than the dry deposition velocities of NO₂ and PAN, similar to the results in Wu et al. (2011) based also on a photosynthesis-based dry deposition model and the flux measurements summarized by Delaria and Cohen (2023).

Many global models have provided their estimates of total and speciated Nr deposition fluxes for previous decades (e.g., Dentener et al., 2006; Paulot et al., 2018; Tan et al., 2018; Rubin et al., 2023). Here, our regional model results present more details which could be beneficial for estimating CL exceedances on relatively smaller spatial scales. They are overall of a lower magnitude, reflecting the impacts of the declining NO_y and Nr emissions which are anticipated to continue into the coming decades. This may also be attributed to the impact of the changing climate and the model uncertainty relevant to scales, deficits in deposition schemes and inputs as well as uncounted deposition of certain organic Nr species due to our chosen chemistry and aerosol schemes. Possibly also for these reasons, a little over 50% of the surface Nr emissions were estimated to be removed via deposition in this area for all years (Fig. 6a), slightly lower than the estimates in previous modeling studies.

405

Comparing our WRF-Chem Nr deposition fluxes to the CL thresholds in Simkin et al. (2016) for herbaceous plants that range from 7.4 to 19.6 kg ha⁻¹ a⁻¹, from 2018 to 2023, the high likelihoods of CL exceedances in Pennsylvania dropped whereas those in parts of North Carolina may have remained high. The Nr deposition fluxes stayed below these CL thresholds over most of the northern forests, a region where primary productivity has been determined to be nitrogen-limited (Du et al., 2020) and can be highly sensitive to the interannual variability in Nr deposition (Fig. S16). The empirical CL thresholds of >3–8 kg ha⁻¹ a⁻¹ for the eastern US forests in Pardo et al. (2011) are higher than the modeled Nr deposition fluxes over the forests in New England states and West Virginia whereas for the other forests roughly close to or lower than the modeled. These results help explain the findings in Horn et al. (2018) that tree growth and survival have increasing and flat-to-slightly-decreasing relationships with Nr deposition for New England/West Virginia forests and other eastern US forests, respectively. For lichen, WRF-Chem suggests that widespread CL exceedances occurred throughout the study period, according to the static CL thresholds of 3.5, 3.1, 1.9, and 1.3 kgN ha⁻¹ a⁻¹ for total species richness, sensitive species richness, forage lichen abundance, and cyanolichen abundance, respectively (Geiser et al., 2019). Note that these lichen CL thresholds are likely to be conservative for the eastern US as they were derived partially from biased model deposition fields, and further assessments on the uncertainty of these thresholds are necessary.

420

3.2 Spatiotemporal variability of Nr and O₃ concentrations and deposition fluxes

The interannual, day-by-day and subdaily variability in HCHO/NO₂ ratios derived from TROPOMI and airborne GCAS and GeoTASO data indicates the variable photochemical environments driven by the changing meteorology and emissions, but, as noted in a number of prior studies (e.g., Duncan et al., 2010; Jin et al., 2017; Tao et al., 2022; Souri et al., 2023), can also be affected by retrieval uncertainty and several other types of errors. Yet, they indicate that, much of the study area belong to NO_x-sensitive or transitional chemical regimes during 2018–2023 (i.e., HCHO/NO₂ higher than empirical thresholds of 2–4, Fig. 9) except very few megacities such as the Greater New York City and Toronto, Canada, and for those urban regions, O₃ formation continues the trends of turning sensitive to NO_x.

430 Largely explainable by the changing NO_y emissions and NO_x -sensitive chemical regimes, the spatial patterns of the modeled interannual differences in column NO_2 and surface O_3 concentrations roughly resemble one another. Both NO_2 and O_3 display downward changes over the majority of terrestrial areas whereas the opposite direction of changes over the Atlantic Ocean (Figs. 7b and 10a). In more than half of the terrestrial model grids, the interannual variability of 19 UTC NO_2 columns and daytime surface O_3 are moderately correlated ($r > 0.6$), with the r value of 0.57 averaged across all overland
435 grids and 0.92 for grids where the p values of the correlation tests are lower than 0.05. Fig. 11 indicates the connection between early afternoon (19 UTC) NO_2 columns and daytime surface O_3 as well as the dependency of this connection on column HCHO/NO_2 ratios. Larger-than-two HCHO/NO_2 values dominate the study region where the overall surface O_3 - NO_2 column spatial correlation is high ($r = 0.54$). Daytime surface O_3 concentrations exhibit the most robust spatial correlation with early afternoon NO_2 columns in 2020 ($r = 0.62$, versus 0.47–0.56 for other years), when the domain-wide median and
440 mean HCHO/NO_2 ratios are larger than the other years' by at least 0.5. These model results suggest that NO_x -sensitive or transitional regimes dominate this region during 2018–2023 and point to a potential of inferring surface O_3 variability across this area from high-quality remote sensing NO_2 and HCHO column data.

The reduction in NO_y emissions contributed to the domain-average changes in median (-0.7 ppbv) and mean (-1.0 ppbv)
445 daytime surface O_3 concentrations overland from 2018 to 2023, which are much smaller than that in 95th% O_3 (by -3.5 ppbv). The lowering NO_y emissions also resulted in less titration, and consequently, the slightly increased 5th% O_3 (by 0.3 ppbv). Such modeled general directions of O_3 temporal changes in this area over the past ~5 years are qualitatively consistent with Cooper et al. (2012) for springs and summers of 1990–2010 as well as follow-on studies (Simon et al., 2015; Lin et al., 2017; Gaudel et al., 2018) and the US EPA's periodically-updated O_3 trend summary (<https://www.epa.gov/air-trends/ozone-trends>, last access: 12 July 2024). The model captured the COVID-induced daytime surface O_3 reductions in 2020 (i.e.,
450 overland, ~0.8 ppbv lower than in 2019 on average) that have also been reported in numerous independent studies (e.g., Keller et al., 2021; Steinbrecht et al., 2021; Putero et al., 2023). The interannual variability of imported O_3 and its precursors from other regions, as well as the interconnected environmental and plant physiological conditions (e.g., via soil-vegetation-atmosphere interactions whose strengths vary in space and time) modulated biogenic VOC emissions, deposition, chemical
455 reactions, transport and mixing, also drove the O_3 changes on regional-to-subregional scales.

The spatial patterns of WRF-Chem modeled surface O_3 broadly match the AQS observations for most of the years (Fig. 10), with root-mean-square errors (RMSEs) ranging from 4.0 to 6.5 ppbv which are significantly lower than the magnitudes of tens of ppbv in many earlier modeling studies for the similar regions. The better performance may have substantially
460 benefited from the advancements in model parameterizations and the updated anth emission inputs. Although WRF-Chem surface and column NO_2 temporal changes agree well with the observed, the model struggled to capture the observed deviations of surface O_3 in 2023 from previous years, likely due to its failure in representing the particularly strong

influences of stratospheric O₃ or/and other extra-regional sources on (near-)surface O₃ in 2023 (Figs. 3b and S2). Later in a case study, the dependency of WRF-Chem O₃ performance on how well transboundary pollution as well as regional climatic conditions and their driving processes are represented in the model will be investigated further.

Similar to dry deposition of Nr species and conclusions from Huang et al. (2022), the spatiotemporal variability of O₃ dry deposition velocities is closely linked with land cover types, environmental and vegetation conditions, with their highest daytime-average values ($v_{d,o_3} > 1.0 \text{ cm s}^{-1}$) seen over moist forests and >30% lower daytime-average values over croplands experiencing drier conditions (Figs. S7 and S15). Cumulative stomatal O₃ uptake (CUO), a recommended metric for assessing the potential O₃ vegetation impact, that is affected by stomatal conductance, boundary layer resistance, and surface O₃ levels, appears also high over the croplands in Ohio and Indiana ($\sim 40 \text{ mmol m}^{-2}$) where surface O₃ concentrations are high while much lower over drier croplands in the Carolinas ($< 30 \text{ mmol m}^{-2}$). Except for regions influenced by the wetter-than-normal conditions or/and increasing surface O₃ concentrations, the CUO fields show declining trends (i.e., overall dropped by $\sim 10\%$ from 2018 to 2023). Our results are qualitatively consistent with those in Clifton et al. (2020) for the northeastern US, where based on a global model, stomatal O₃ uptake cumulated through MJJ 2010 with no detoxification threshold was estimated to be $\sim 35 \text{ mmol m}^{-2}$. Their modeled flux was projected to decrease under the Representative Concentration Pathways 8.5 future scenario under which soil may be drier than present day conditions over the eastern US (Cook et al., 2020). As indicated in Fig. 12a, our modeled CUO values are higher over croplands and forests than shrub/grass averagely and more spatially variable. These CUO fluxes display clearer trends in most grids than the total Nr deposition fluxes, due to NO_y and NH_x deposition fluxes having competing directions of changes through the past years (Figs. 8b–c and S15). The potential impacts of Nr deposition are strongest and weakest on croplands and water, respectively (Fig. 12b).

3.3 Three case studies

3.3.1 Land DA

Satellite (i.e., GPM, SMAP, and TROPOMI) and in situ observations collected at/round Harvard Forest and the CRN-Millbrook site during the SMAPVEX22 campaign were analyzed along with WRF-Chem results during a precipitating event associated with a frontal passage that occurred from late 13 July to early 14 July 2022. This event caused sharp increases in SSM around 14 July in Massachusetts (by $> 0.06 \text{ m}^3 \text{ m}^{-3}$) and parts of the eastern New York (by $\sim 0.02 \text{ m}^3 \text{ m}^{-3}$), as well as drastic changes in air temperature (by up to $\sim 5 \text{ K}$ decreases at the surface) and other meteorological fields. These changes in SSM and meteorological conditions contributed to abrupt O₃ reductions of up to 30 ppbv. Baseline simulation without DA failed to reproduce the strong daily SSM variability at site-to-regional scales (Fig. 13b). After enabling the SMAP DA, Noah-MP SSM in Massachusetts and the eastern New York increased remarkably on 14 July (Fig. 13c), better matching the observed quantities. Along the southern New York-Connecticut as well as the northern New York-Vermont borders, the slightly drier conditions on 14 July are also better represented in Noah-MP with the implementation of SMAP DA (Fig. 13a–c). The enhancements in soil wetness resulted in altered precipitation characteristics, a bit cooler surface soil/air, thinner

atmospheric boundary layer, suppressed biogenic VOC and soil NO_y emissions as well as O₃ formation while deposition accelerated. Lightning emissions were also sensitive to the DA-induced SM changes. Consequently, above many Connecticut River watershed areas, WRF-Chem NO₂ columns dropped (Fig. 13e–f). Due to increased upwind pollution contributions whereas weakened local emissions and production, both enhancements and reductions by up to ~4 ppbv in daytime surface O₃ levels (not shown in figures) are found in the New England region (40.5–43.1°N, 70.0–74.0°W). Across the New England region, WRF-Chem daytime surface O₃ performance for 14 July was improved in 31 out of 50 of the model grids where AQS data were available, with the largest improvement of nearly 2 ppbv. It is also highlighted that the various processes SM can impact help shape the vertical profiles of NO₂ and other chemical species, a critical ancillary data for calculating the air mass factor that is needed to convert slant columns to vertical columns in satellite retrievals (Lorente et al., 2017) and derive averaging kernels (AKs, Eskes and Boersma, 2003). At Harvard Forest, the vertical distributions of NO₂ as well as their responses to SMAP DA changed rapidly during this event (Fig. 13g–h), despite the minor change in NO₂ column. It is suggested that cautions are taken when attributing the mismatches between TROPOMI and models (with AKs, that indicate lower TROPOMI sensitivity towards the surface) over the scenes where NO_x near the surface and aloft may both be significant. Also, productions, interpretations, and applications of satellite NO₂ retrievals could benefit from evaluating and tuning their model-based *a priori* profiles with in situ measurements of NO₂ vertical distributions under various environments.

Figure 14a–c illustrates that, on a larger timescale, SMAP DA effectively narrowed the Noah-MP wet biases in July 2022–July 2018 SSM differences in Canada’s Ontario (croplands) as well as the dry biases in Virginia (forests) that may have resulted from inaccurate representations of meteorological drought conditions. WRF-Chem weather fields, biogenic VOC, soil NO_y and lightning emissions, and deposition processes all responded to the DA-induced changes in the model’s land ICs. The July 2022–July 2018 differences of WRF-Chem NO₂ columns and surface O₃ over these regions became closer to (by as high as ~50% and >4 ppbv, respectively) what TROPOMI and AQS observations indicate (Fig. 14d–i). Notably, the SMAP DA flipped the sign of surface O₃ interannual differences over the northern Virginia, for which region the DA had strong impacts on the modeled surface O₃ in both July 2018 and July 2022 (Fig. S18). The remaining modeled-observed NO₂ and O₃ discrepancies over some of the northern states and coastal North Carolina, which are highly correlated because of the dominating NO_x-limited regime, can also be explained by uncertainties in the model’s chemical BCs and wind fields.

These analyses demonstrate that microwave satellite SM DA can improve the modeled SM dynamics at daily-to-interannual timescales. Similar findings were previously reported by Draper and Reichle (2015) where SM from the X-band (sensitive to top ~1 cm soil) Advanced Microwave Scanning Radiometer–Earth Observing System was assimilated at only four sites, but not on regional scales for forested regions where SM retrievals have been considered challenging and need validation. It is also shown in this work that the DA adjustments to LSMs’ SM fields can positively impact weather and chemistry fields from their coupled atmospheric models, benefiting our interpretations and prediction skills of air pollutants’ distributions and

temporal changes which can in turn help advance satellite retrievals. It is important to note that SSM-atmosphere coupling strengths vary strongly in space and time, influenced by the evolution of local hydrological regimes. As 2022-2018 SSM and surface air temperature differences show strong negative correlations of -0.78 (Fig. S19), the land DA impacts on WRF-Chem's atmospheric chemistry fields were in some part through adjusting the weather, as indicated in Figs. 14j-l and S18. 535 For the times/locations that SSM and atmosphere coupling strengths are weak, land DA is anticipated to impact the modeled atmospheric chemistry fields mostly via the direct control of land surface on natural emissions and deposition.

3.3.2 Irrigation approaches

Based on the three sets of simulations representing full-, reduced-, and no-irrigation scenarios (Section 2.3.2), the impacts of irrigation on surface O₃ concentrations, CUO and O₃ injury to vegetation, as well as Nr deposition were quantified (Fig. 15). 540 Across the domain, O₃ perturbs gross primary productivity more strongly (up to 20–30%) than transpiration (mostly <10%), and therefore reduces the vegetation water use efficiency. Its reductions to leaf biomass over the stressed irrigated lands in the Carolinas in late June 2022 are estimated to be <5% under all three scenarios. Under the limited- and no-irrigation conditions, O₃-induced crop yield losses were reduced over irrigated areas by up to ~2%, a result of lowered SM (Fig. S20) 545 and deposition fluxes despite the enhanced soil/air temperatures, soil NO_y emissions and surface O₃ concentrations (by up to ~10 ppbv). This result supports and extends the findings from previous coarse-resolution modeling (Mills et al., 2018) and observational (Harmens et al., 2019) studies. The period-integrated O₃ stomatal uptake increased slightly outside of the irrigated land due to higher O₃ being transported away from the irrigated areas. Over/near the irrigated areas, the estimated total Nr deposition would also be lower under reduced- and no-irrigation scenarios by more than 50%, which would be 550 below possible CL thresholds, as less irrigation would result in stronger atmospheric mixing and reduced SM although soil NO_y emissions would increase. These impacts on Nr deposition over most of the irrigated lands are important also according to Student's *t*-tests comparing the base and sensitivity simulations ($p < 0.05$). The impacts of irrigation on Nr deposition over non-irrigated areas are rather noisy and more intense than on O₃, where Student's *t*-tests comparing Nr deposition from different simulations gave larger-than-0.05 *p* values. These sensitivities away from irrigated lands still highlight the complex 555 net effects of irrigation-induced changes in land surface and meteorological conditions on a group of species with substantially different properties undergoing various atmospheric processes.

Compared with long-term offline LSM simulations forced by independently produced O₃ data, evaluations of O₃ vegetation impacts using coupled modeling systems like WRF-Chem with land surface feedback to regional weather and atmospheric 560 chemistry being accounted for are more realistic. Nevertheless, such approaches are hundreds of times more computationally expensive and may be subject to uncertainty from the atmospheric model. Survey- and satellite-based irrigation types and water use information, including wastewater use that may impact plant growth, nutrient supply and soil environments (Aman et al., 2018), direct stationary and/or airborne measurements of water, carbon, energy, air pollutants' concentrations and fluxes, as well as plant traits within and outside of irrigated areas for variable hydroclimatic conditions, would help evaluate

565 and improve irrigation modeling and the model-based holistic assessments of irrigation impacts on regional environments
that could assist with forming pollution mitigation and ecosystem adaptation strategies for future.

3.3.3 Transboundary pollution

Periodically, distant pollution sources make strong environmental impacts on the Northeast and Mid-Atlantic US states. For
570 example, during the 2023 SARP-East campaign, JPSS-1/CrIS observed high O₃ and low CO on 13 June; and high O₃, CO,
and PAN on the following days of the same week (Fig. 16) when elevated NH₃ columns and aerosol optical depths were also
observed from space by multiple instruments (not shown). These data suggest that long-range transported stratospheric air
and Canadian wildfire plumes reached the eastern US.

575 As indicated by the stratospheric O₃ tracer of the chemical BC model WACCM, the 13 June stratospheric intrusion event
associated with a frontal passage enhanced lower tropospheric O₃ by as high as 30–40 ppbv along the northeast corridor,
which helps explain the spike at ~700 hPa (>30 ppbv O₃ enhancement) in the SARP-East RRC ozonesonde profile for that
day (Fig. 17a–b). The WACCM-estimated stratospheric impact on surface O₃ in our WRF-Chem domain is only ¼–1/3 of its
impact on free tropospheric O₃ (Fig. S21), consistent with prior knowledge that stratospheric impacts on the US East are
580 often confined at higher altitudes while surface O₃ remains low (Ott et al., 2016). Thick Canadian wildfire plumes that
moved into the study region, dramatically enhanced O₃ spanning a wide altitude range (i.e., from >900 hPa to ~600 hPa)
above the RRC site on several days of that week (Fig. 17b). Under the strong influences of Canadian fires, O₃ in the US
outflows during that week was close to that in the air sampled ~two decades ago along the East Coast (Cooper et al., 2005).
Ozonesondes also indicate that air quality improved remarkably in the following week, with O₃ from the surface to ~700 hPa
585 nearly 40 ppbv lower (Fig. 17b).

The WRF-Chem baseline and “Sen” sensitivity simulations were evaluated with O₃ observations during 13–16 June 2023.
Overall, the baseline and “Sen” simulations moderately well reproduced the daytime surface O₃ patterns and diurnal cycles
observed at AQS sites during the events, with RMSEs of ~7 ppbv (Figs. 17c–k and S21). The negative mean biases of 1–2
590 ppbv in the modeled daytime peak O₃ (Fig. 17c) can be explained by the model’s incapability of accurately representing the
stratospheric O₃ influences. The choice of WACCM’s fire emission input had minor impacts on WRF-Chem daytime surface
O₃ averaged across the domain throughout the episode but enhanced/reduced WRF-Chem’s daily daytime surface O₃ by up
to ~10 ppbv on grid scale (Figs. S21–S22).

595 The extremely high transported background aerosols and their precursors due to Canadian wildfires, along with upwind US
pollution, interacted with meteorological and land surface fields (e.g., radiation, temperature, clouds, precipitation, and
surface wetness) that are relevant to evapotranspiration and photosynthesis (see also discussions on Asian anth pollution
impacts in Huang et al., 2020, and references therein), dry deposition velocity and wet deposition coefficient, and secondary

pollutant formation. The baseline and “Clean BC” cases together indicate that, although under highly polluted conditions, dry deposition velocities are overall reduced (Fig. S23) and photochemistry activities are weakened, the period-integrated CUO and mean total Nr deposition fluxes are enhanced as the excessive amount of imported pollution significantly elevated surface O₃ and Nr concentrations (Fig. 18). During this period, daily O₃ stomatal uptake and the mean total Nr deposition overland are ~2% and ~26% higher than their 2023 seasonal-mean values, respectively. Comparisons of baseline and “Sen” simulations results show that the modeled grid-scale O₃ stomatal uptake and total Nr deposition are sensitive to the choice of WACCM’s fire emission input (Fig. S22). This set of sensitivity analysis not only supports the findings about fire emission impacts on deposition from offline air quality modeling studies (e.g., Koplitz et al., 2021), but also stresses the importance of accounting for aerosol radiative effects in assessing ecosystem impacts of pollutants from biomass burning and other sources, which will be investigated further on multiple spatiotemporal scales in an Hemispheric Transport of Air Pollution phase 3 multimodel experiment (Whaley et al., 2024, <https://doi.org/10.5194/gmd-2024-126>, in review).

Previous work has focused strongly on the impacts of long-range transport of pollution from Asia and the stratosphere, as well as regional pollution transport, on the western US O₃ trends (e.g., Cooper et al., 2012; Huang et al., 2013; Lin et al., 2017; Miyazaki et al., 2022). This case study demonstrates that extra-regional pollution can also compromise the efforts of improving air quality via controlling local and regional emissions over the eastern US. Possibly linked to climate change, such highly polluted events occurred more frequently during the 2023 warm season. For example, driven by hot and dry conditions, the Canadian 2023 wildfire season had the largest area burned in history (<https://cwfis.cfs.nrcan.gc.ca/ha/nfdb>, last access: 23 July). Due to Canadian wildfire impacts, there were at least two other known extreme air pollution events over the eastern US in June 2023 and more in the other months of the season (Fig. S24). Such events exerted controls on surface-atmosphere exchange processes and perturbing the long-term changes in O₃, Nr and other chemical compounds. More accurate and consistently-configured chemical BC models or reanalysis products, preferably at higher resolutions with a more complete list of prognostic and diagnostic variables, are essential for further regional-scale modeling investigations on such events and their contributions to trends/variability. Addition of stratospheric tracers and accurate, time-varying upper chemical boundary conditions to regional models, assisted with O₃ profile measurements from commercial aircraft, sondes, and Lidar networks, are expected to be also helpful for diagnosing and/or reducing errors in the simulations of some of such events.

4 Summary and suggested future directions

Based on WRF-Chem model simulations and multiplatform observations, this paper discussed Nr and O₃ concentrations and fluxes during 2018–2023 in the northeastern and mid-Atlantic US, most of which fell into NO_x-limited and transitional chemical regimes. Effective local emission controls resulted in evident decreases in NO₂ and surface O₃ concentrations, with the reduced human activities during the COVID lockdowns also contributing to their low values and the overall stronger surface O₃-NO₂ column correlations in 2020. Current polar-orbiting satellites take snapshots of NO₂ columns only at a

particular time of day, such as in the early afternoon when surface NO₂ experienced their daily lows. With this sparse temporal sampling, TROPOMI did not miss the general NO₂ interannual and seasonal variability and filled in the extremely large horizontal gaps between surface AQS observations most of which are in/near urban regions and positively biased. The WRF-Chem simulation described here has been extended into 2024, running on a routine basis, to support refined analyses concerning the subdaily variability of NO₂ and other variables along with data from geostationary satellite missions such as the TEMPO.

The declines in NO_y emissions and concentrations were roughly consistent with the temporal changes in NO_y deposition, which were balanced out by the overall rising agricultural and total NH_x emissions and deposition. The changes in NO_y and NH_x deposition together shaped the interannual variability in Nr deposition in contrast to the clearer downward trends in O₃ vegetation uptake that reduced plants' water use efficiency and caused biomass/crop yield losses by a few percent. Certain hotspots of Nr deposition in North Carolina may have continued to exceed the CL thresholds for herbaceous plants and trees in literature, while the productivity of northern forests may have remained to be nitrogen-limited. Referring to the conservative lichen CL thresholds in literature, widespread lichen CL exceedances likely occurred persistently. Integrating nitrogen dynamics into LSMs could help improve their performance on land surface states as well as carbon, water, and energy fluxes, and further, the representations of Nr and O₃ deposition processes and their interactions in coupled modeling systems. Standard versions of Noah-MP, including what was used in this work, represent nitrogen stress by applying constant foliage nitrogen factors (<1) in maximum carboxylation rate calculations (Niu et al., 2011). Following the JULES and Community Land Model, Cai et al. (2016) started to add nitrogen dynamics to Noah-MP. Running offline, their updated model yielded more accurate net primary productivity and evapotranspiration, and that may also be embedded into Earth system models in future, with the magnitudes and spatiotemporal variability of its Nr inputs (e.g., from deposition and fertilizer applications) being improved with the aid of atmospheric chemistry model routines or/and observations. Other areas for improvements include assimilating additional Earth observations (e.g., rootzone SM and terrestrial water storage); developing and applying high-quality, spatially and temporally varying CO₂ forcings for Noah-MP; and tuning parameters that represent O₃ vegetation impacts for various types of plants at different growth stages.

With updated model parameterizations and anth emissions, the used WRF-Chem system performed stably and remarkably better on eastern US surface O₃ than many of those in literature. This paper highlighted that, temporal variability of Nr and O₃ concentrations and fluxes on subregional-to-local scales were partially driven by hydrological variability that can be influenced by precipitation and controllable human activities such as irrigation. Like deposition processes, biogenic soil Nr and VOC emissions that are highly sensitive to various climatic factors and plants' physiological conditions, as well as extra-regional sources (e.g., dense wildfire plumes from the western US and Canada, and O₃-rich stratospheric air), have been playing increasingly important roles in controlling pollutants' budgets in this area as local emissions went down. These outcomes based on this particular WRF-Chem system have implications for updating other modeling systems.

It is worth noting that, urban emissions and air pollutants can be transported to and deposited into rural and remote regions, which may better be modeled at finer resolutions (e.g., urban scale at 1–4 km or street-to-building scales) with the urban landscapes and human influences on urban vegetation and soil properties being more carefully handled. Finer model resolutions may also allow more processes, such as convection, to be explicitly resolved, potentially leading to more accurate precipitation and deposition results. Successful finer-resolution simulations would require accurate inputs and observational constraints at similar resolutions. To better inform the designs of mitigation and adaptation strategies, it is highly recommended to continue evaluating and improving the parameterizations and inputs relevant to various sources and processes in seamlessly coupled multiscale Earth system models using laboratory and field experiments in combination with satellite DA. Further improved Earth system model results are expected to in turn benefit remote sensing communities, for example, via serving as the retrieval *a priori* profiles for different types of environments.

Code and data availability

NASA-Unified Weather Research and Forecasting model (<https://nuwrf.gsfc.nasa.gov/software>, last access: 6 February 2024) output of O₃ and other key variables will be shared via Zenodo with the final version of this manuscript. Remote sensing and in situ data sets can be downloaded from: <https://doi.org/10.5067/4DQ54OUIJ9DL> (O’Neill et al., 2021), <https://doi.org/10.5067/GPM/IMERGDF/DAY/07> (Huffman et al., 2023); <https://doi.org/10.5067/MHH8R0UZ5BMJ> (Bowman, 2022a); <https://doi.org/10.5067/JL1HT3NGEAW3> (Bowman, 2022b); <https://doi.org/10.5067/6HTQB4F81S08> (Bowman, 2022c); <https://www-air.larc.nasa.gov/cgi-bin/ArcView/listos> (Janz, 2020); <https://doi.org/10.5065/4F4P-E398> (NCEP, 2004); and https://aqs.epa.gov/aqsweb/airdata/download_files.html (US EPA, 2024, last access: 1 October 2024). Gridded TROPOMI data have been submitted by Isabelle De Smedt to TOAR-II Tropospheric Ozone Precursors Focus Group repository.

Author contributions

Overall study design and paper writing: MH leading, all participated in reviewing and editing
Design, execution, or discussions of model simulations: MH, GRC, SVK, ABG
Satellite data production, validation, delivery, and analysis: KWB, IDS, AC, MHC, MH
Field campaign deployments and data analysis: AC, MHC, SJJ, RMS, AMT, NMF, RJS, JDB, ATJ, MH

Competing interests

The authors declare that they have no competing interests.

Acknowledgements

695 NASA SMAP, SMAPVEX22 and LDAS sponsored part of the work. A contribution was made to this work at the Jet Propulsion Laboratory, California Institute of Technology, under a contract with NASA. We acknowledge the excellent leadership of TOAR-II Tropospheric Ozone Precursors and Deposition Focus Group leads. We thank Antonin Soulie and team for helping with the CAMS global anth emissions, and Kyle DeLong for participating in collecting SM data in Harvard Forest during SMAPVEX22 that are used in this study. Color palettes in Crameri et al. (2020) are used in this paper.

700 References

- Aman, M. S., Jafari, M., Reihan, M. K., Motesharezadeh, B., and Zare, S.: Assessing the Effect of Industrial Wastewater on Soil Properties and Physiological and Nutritional Responses of Robinia Pseudoacacia, Cercis Siliquastrum and Caesalpinia Gilliesii Seedlings, *J. Environ. Manag.*, <https://doi.org/10.1016/j.jenvman.2018.03.087>, 217, 718–726, 2018.
- 705 Bowman, K. W.: TROPES CrIS-JPSS1 L2 Ozone for Forward Stream Summary Product, Version 1, Greenbelt, MD, USA, Goddard Earth Sciences Data and Information Services Center (GES DISC) [data set], Greenbelt, Maryland, USA, <https://doi.org/10.5067/MHH8R0UZ5BMJ>, 2022a.
- Bowman, K. W.: TROPES CrIS-JPSS1 L2 Carbon Monoxide for Forward Stream Summary Product, Version 1, Greenbelt,
710 MD, USA, Goddard Earth Sciences Data and Information Services Center (GES DISC) [data set], Greenbelt, Maryland, USA, <https://doi.org/10.5067/JL1HT3NGEAW3>, 2022b.
- Bowman, K. W.: TROPES CrIS-JPSS1 L2 Peroxyacetyl Nitrate for Forward Stream Summary Product, Version 1,
715 Maryland, USA, <https://doi.org/10.5067/6HTQB4F81S08>, 2022c.
- Cai, X., Yang, Z.-L., Fisher, J. B., Zhang, X., Barlage, M., and Chen, F.: Integration of nitrogen dynamics into the Noah-MP land surface model v1.1 for climate and environmental predictions, *Geosci. Model Dev.*, 9, 1–15, <https://doi.org/10.5194/gmd-9-1-2016>, 2016.
- 720 Carlton, A. G., Pinder, R. W., Bhave, P. V., and Pouliot, G. A.: To What Extent Can Biogenic SOA be Controlled? *Environ. Sci. Technol.*, 44, 3376–3380, <https://doi.org/10.1021/es903506b>, 2010.

- 725 Chai, T., Carmichael, G. R., Tang, Y., Sandu, A., Hardesty, M., Pilewskie, P., Whitlow, S., Browell, E. V., Avery, M. A.,
Nédélec, P., Merrill, J. T., Thompson, A. M., and Williams, E.: Four-dimensional data assimilation experiments with
International Consortium for Atmospheric Research on Transport and Transformation ozone measurements, *J. Geophys.*
Res., 112, D12S15, <https://doi.org/10.1029/2006JD007763>, 2007.
- 730 Chai, T., Kim, H.-C., Lee, P., Tong, D., Pan, L., Tang, Y., Huang, J., McQueen, J., Tsidulko, M., and Stajner, I.: Evaluation
of the United States National Air Quality Forecast Capability experimental real-time predictions in 2010 using Air Quality
System ozone and NO₂ measurements, *Geosci. Model Dev.*, 6, 1831–1850, <https://doi.org/10.5194/gmd-6-1831-2013>, 2013.
- 735 Clifton, O. E., Lombardozzi, D. L., Fiore, A. M., Paulot, F., and Horowitz, L. W.: Stomatal conductance influences
interannual variability and long-term changes in regional cumulative plant uptake of ozone, *Environ. Res. Lett.*, 15, 114059,
<https://doi.org/10.1088/1748-9326/abc3f1>, 2020.
- 740 Colarco, P. R., Schoeberl, M. R., Doddridge, B. G., Marufu, L. T., Torres, O., and Welton, E. J.: Transport of smoke from
Canadian forest fires to the surface near Washington, D.C.: Injection height, entrainment, and optical properties, *J. Geophys.*
Res., 109, D06203, <https://doi.org/10.1029/2003JD004248>, 2004.
- Cook, B. I., Mankin, J. S., Marvel, K., Williams, A. P., Smerdon, J. E., and Anchukaitis, K. J.: Twenty-first century drought
projections in the CMIP6 forcing scenarios, *Earth's Future*, 8, e2019EF001461, <https://doi.org/10.1029/2019EF001461>,
2020.
- 745 Cooper, O. R., Stohl, A., Eckhardt, S., Parrish, D. D., Oltmans, S. J., Johnson, B. J., Nédélec, P., Schmidlin, F. J.,
Newchurch, M. J., Kondo, Y., and Kita, K.: A springtime comparison of tropospheric ozone and transport pathways on the
east and west coasts of the United States, *J. Geophys. Res.*, 110, D05S90, <https://doi.org/10.1029/2004JD005183>, 2005.
- 750 Cooper, O. R., Gao, R.-S., Tarasick, D., Leblanc, T., and Sweeney, C.: Long-term ozone trends at rural ozone monitoring
sites across the United States, 1990–2010, *J. Geophys. Res.*, 117, D22307, <https://doi.org/10.1029/2012JD018261>, 2012.
- Cramer, F., Shephard, G. E., and Heron, P. J.: The misuse of colour in science communication, *Nat. Commun.*, 11, 5444,
<https://doi.org/10.1038/s41467-020-19160-7>, 2020.

- 755 Darmenov, A. and da Silva, A.: The Quick Fire Emissions Dataset (QFED): Documentation of versions 2.1, 2.2 and 2.4, NASA Technical Report Series, Global Modeling and Data Assimilation, NASA TM-2015-104606/Volume 38, available at: <http://gmao.gsfc.nasa.gov/pubs/docs/Darmenov796.pdf> (last access: 12 January 2023), 2015.
- De Smedt, I., Pinardi, G., Vigouroux, C., Compernelle, S., Bais, A., Benavent, N., Boersma, F., Chan, K.-L., Donner, S.,
760 Eichmann, K.-U., Hedelt, P., Hendrick, F., Irie, H., Kumar, V., Lambert, J.-C., Langerock, B., Lerot, C., Liu, C., Loyola, D.,
Piters, A., Richter, A., Rivera Cárdenas, C., Romahn, F., Ryan, R. G., Sinha, V., Theys, N., Vlietinck, J., Wagner, T., Wang,
T., Yu, H., and Van Roozendael, M.: Comparative assessment of TROPOMI and OMI formaldehyde observations and
validation against MAX-DOAS network column measurements, *Atmos. Chem. Phys.*, 21, 12561–12593,
<https://doi.org/10.5194/acp-21-12561-2021>, 2021.
- 765 Dentener, F., Drevet, J., Lamarque, J. F., Bey, I., Eickhout, B., Fiore, A. M., Hauglustaine, D., Horowitz, L. W., Krol, M.,
Kulshrestha, U. C., Lawrence, M., Galy-Lacaux, C., Rast, S., Shindell, D., Stevenson, D., Van Noije, T., Atherton, C., Bell,
N., Bergman, D., Butler, T., Cofala, J., Collins, B., Doherty, R., Ellingsen, K., Galloway, J., Gauss, M., Montanaro, V.,
Müller, J. F., Pitari, G., Rodriguez, J., Sanderson, M., Solmon, F., Strahan, S., Schultz, M., Sudo, K., Szopa, S., and Wild,
770 O.: Nitrogen and sulfur deposition on regional and global scales: A multimodel evaluation, *Global Biogeochem. Cy.*, 20,
B4003, <https://doi.org/10.1029/2005GB002672>, 2006.
- Delaria, E. R. and Cohen, R. C.: Measurements of Atmosphere–Biosphere Exchange of Oxidized Nitrogen and Implications
for the Chemistry of Atmospheric NO_x, *Acc. Chem. Res.*, 56, 1720–1730, <https://doi.org/10.1021/acs.accounts.3c00090>,
775 2023.
- Dix, B., Francoeur, C., Li, M., Serrano-Calvo, R., Levelt, P. F., Veeckind, J. P., McDonald, B. C., and de Gouw, J.:
Quantifying NO_x Emissions from U.S. Oil and Gas Production Regions Using TROPOMI NO₂, *ACS Earth and Space
Chem.*, 6, 403–414, <https://doi.org/10.1021/acsearthspacechem.1c00387>, 2022.
- 780 Doumbia, T., Granier, C., Elguindi, N., Bouarar, I., Darras, S., Brasseur, G., Gaubert, B., Liu, Y., Shi, X., Stavrakou, T.,
Tilmes, S., Lacey, F., Deroubaix, A., and Wang, T.: Changes in global air pollutant emissions during the COVID-19
pandemic: a dataset for atmospheric modeling, *Earth Syst. Sci. Data*, 13, 4191–4206, [https://doi.org/10.5194/essd-13-4191-
2021](https://doi.org/10.5194/essd-13-4191-2021), 2021.
- 785 Draper, C. and Reichle, R.: The impact of near-surface soil moisture assimilation at subseasonal, seasonal, and inter-annual
timescales, *Hydrol. Earth Syst. Sci.*, 19, 4831–4844, <https://doi.org/10.5194/hess-19-4831-2015>, 2015.

- 790 Du, E., Terrer, C., Pellegrini, A.F.A., Ahlström, A., van Lissa, C. J., Zhao, X., Xia, N., Wu, X., and Jackson, R. B.: Global patterns of terrestrial nitrogen and phosphorus limitation, *Nat. Geosci.*, 13, 221–226, <https://doi.org/10.1038/s41561-019-0530-4>, 2020.
- 795 Duncan, B. N., Yoshida, Y., Olson, J. R., Sillman, S., Martin, R. V., Lamsal, L., Hu, Y., Pickering, K. E., Retscher, C., Allen, D. J., and Crawford, J. H.: Application of OMI observations to a space-based indicator of NO_x and VOC controls on surface ozone formation, *Atmos. Environ.*, 44, 2213–2223, <https://doi.org/10.1016/j.atmosenv.2010.03.010>, 2010.
- 800 Dunlea, E. J., Herndon, S. C., Nelson, D. D., Volkamer, R. M., San Martini, F., Sheehy, P. M., Zahniser, M. S., Shorter, J. H., Wormhoudt, J. C., Lamb, B. K., Allwine, E. J., Gaffney, J. S., Marley, N. A., Grutter, M., Marquez, C., Blanco, S., Cardenas, B., Retama, A., Ramos Villegas, C. R., Kolb, C. E., Molina, L. T., and Molina, M. J.: Evaluation of nitrogen dioxide chemiluminescence monitors in a polluted urban environment, *Atmos. Chem. Phys.*, 7, 2691–2704, <https://doi.org/10.5194/acp-7-2691-2007>, 2007.
- 805 Elguindi, N., Granier, C., Stavrou, T., Darras, S., Bauwens, M., Cao, H., Chen, C., Denier van der Gon, H. A. C., Dubovik, O., Fu, T. M., Henze, D. K., Jiang, Z., Keita, S., Kuenen, J. J. P., Kurokawa, J., Liousse, C., Miyazaki, K., Müller, J. F., Qu, Z., Solomon, F., and Zheng, B.: Intercomparison of Magnitudes and Trends in Anthropogenic Surface Emissions From Bottom-Up Inventories, Top-Down Estimates, and Emission Scenarios, *Earths Future*, 8, e2020EF001520, <https://doi.org/10.1029/2020EF001520>, 2020.
- 810 Emberson, L.: Effects of ozone on agriculture, forests and grasslands, *Phil. Trans. R. Soc. A.*, 378, 20190327, <https://doi.org/10.1098/rsta.2019.0327>, 2020.
- 815 Erisman, J. W., Van Pul, A., and Wyers, P.: Parameterization of surface resistance for the quantification of atmospheric deposition of acidifying pollutants and ozone, *Atmos. Environ.*, 28, 2595–2607, [https://doi.org/10.1016/1352-2310\(94\)90433-2](https://doi.org/10.1016/1352-2310(94)90433-2), 1994.
- 820 Eskes, H. J. and Boersma, K. F.: Averaging kernels for DOAS total-column satellite retrievals, *Atmos. Chem. Phys.*, 3, 1285–1291, <https://doi.org/10.5194/acp-3-1285-2003>, 2003.
- Felzer, B. S., Cronin, T. W., Melillo, J. M., Kicklighter, D. W., and Schlosser, C. A.: Importance of carbon-nitrogen interactions and ozone on ecosystem hydrology during the 21st century, *J. Geophys. Res.*, 114, G01020, <https://doi.org/10.1029/2008JG000826>, 2009.

Fiore, A. M., Dentener, F. J., Wild, O., Cuvelier, C., Schultz, M. G., Hess, P., Textor, C., Schulz, M., Doherty, R. M., Horowitz, L. W., MacKenzie, I. A., Sanderson, M. G., Shindell, D. T., Stevenson, D. S., Szopa, S., van Dingenen, R., Zeng,
825 G., Atherton, C., Bergmann, D., Bey, I., Carmichael, G., Collins, W. J., Duncan, B. N., Faluvegi, G., Folberth, G., Gauss, M., Gong, S., Hauglustaine, D., Holloway, T., Isaksen, I. S. A., Jacob, D. J., Jonson, J. E., Kaminski, J. W., Keating, T. J., Lupu, A., Marmmer, E., Montanaro, V., Park, R. J., Pitari, G., Pringle, K. J., Pyle, J. A., Schroeder, S., Vivanco, M. G., Wind, P., Wojcik, G., Wu, S., and Zuber, A.: Multimodel estimates of intercontinental source-receptor relationships for ozone pollution, *J. Geophys. Res.*, 114, D04301, <https://doi.org/10.1029/2008JD010816>, 2009.

830

Fu, J. S., Carmichael, G. R., Dentener, F., Aas, W., Andersson, C., Barrie, L. A., Cole, A., Galy-Lacaux, C., Geddes, J., Itahashi, S., Kanakidou, M., Labrador, L., Paulot, F., Schwede, D., Tan, J., and Vet, R.: Improving Estimates of Sulfur, Nitrogen, and Ozone Total Deposition through Multi-Model and Measurement-Model Fusion Approaches, *Environ. Sci. Technol.*, 56, 2134–2142, <https://doi.org/10.1021/acs.est.1c05929>, 2022.

835

Galloway, J. N., Aber, J. D., Erisman, J. W., Seitzinger, S. P., Howarth, R. W., Cowling, E. B., and Cosby, B. J.: The nitrogen cascade, *Bioscience*, 53, 341–356, [https://doi.org/10.1641/0006-3568\(2003\)053\[0341:TNC\]2.0.CO;2](https://doi.org/10.1641/0006-3568(2003)053[0341:TNC]2.0.CO;2), 2003.

Galloway, J. N., Dentener, F. J., Capone, D. G., Boyer, E. W., Howarth, R. W., Seitzinger, S. P., Asner, G. P., Cleveland, C.
840 C., Green, P. A., Holland, E. A., Karl, D. M., Michaels, A. F., Porter, J. H., Townsend, A. R., and Vorosmarty, C. J.: Nitrogen cycles: past, present, and future, *Biogeochemistry*, 70, 153–226, <https://doi.org/10.1007/s10533-004-0370-0>, 2004.

Gaudel, A., Cooper, O. R., Ancellet, G., Barret, B., Boynard, A., Burrows, J. P., Clerbaux, C., Coheur, P. F., Cuesta, J., Cuevas, E., Doniki, S., Dufour, G., Ebojje, F., Foret, G., Garcia, O., Granados-Munoz, M. J., Hannigan, J. W., Hase, F.,
845 Hassler, B., Huang, G., Hurtmans, D., Jaffe, D., Jones, N., Kalabokas, P., Kerridge, B., Kulawik, S., Latter, B., Leblanc, T., Le Flochmoen, E., Lin, W., Liu, J., Liu, X., Mahieu, E., McClure-Begley, A., Neu, J. L., Osman, M., Palm, M., Petetin, H., Petropavlovskikh, I., Querel, R., Rapp, N., Rozanov, A., Schultz, M. G., Schwab, J., Siddans, R., Smale, D., Steinbacher, M., Tanimoto, H., Tarasick, D. W., Thouret, V., Thompson, A. M., Trickl, T., Weatherhead, E., Wespes, C., Worden, H. M., Vigouroux, C., Xu, X., Zeng, G., and Ziemke, J.: Tropospheric Ozone Assessment Report: Present-day distribution and
850 trends of tropospheric ozone relevant to climate and global atmospheric chemistry model evaluation, *Elementa-Sci. Anthropol.*, 6, 39, <https://doi.org/10.1525/elementa.291>, 2018.

Geddes, J. A. and Martin, R. V.: Global deposition of total reactive nitrogen oxides from 1996 to 2014 constrained with satellite observations of NO₂ columns, *Atmos. Chem. Phys.*, 17, 10071–10091, <https://doi.org/10.5194/acp-17-10071-2017>,
855 2017.

Geiser, L. H., Nelson, P. R., Jovan, S. E., Root, H. T., and Clark, C. M.: Assessing Ecological Risks from Atmospheric Deposition of Nitrogen and Sulfur to US Forests Using Epiphytic Macrolichens, *Diversity*, 2019; 11, 87, <https://doi.org/10.3390/d11060087>, 2019.

860

Georgoulas, A. K., Boersma, K. F., van Vliet, J., Zhang, X., van der A, R., Zanis, P., and de Laat, J.: Detection of NO₂ pollution plumes from individual ships with the TROPOMI/S5P satellite sensor, *Environ. Res. Lett.*, 15, 124037, <https://doi.org/10.1088/1748-9326/abc445>, 2020.

865 Goldberg, D. L., Anenberg, S. C., Kerr, G. H., Moheg, A., Lu, Z., and Streets, D. G.: TROPOMI NO₂ in the United States: A detailed look at the annual averages, weekly cycles, effects of temperature, and correlation with surface NO₂ concentrations, *Earth's Future*, 9, e2020EF001665, <https://doi.org/10.1029/2020EF001665>, 2021.

870 Granier, C., S. Darras, H. Denier van der Gon, J. Doubalova, N. Elguindi, B. Galle, M. Gauss, M. Guevara, J.-P. Jalkanen, J. Kuenen, C. Lioussé, B. Quack, D. Simpson, K. Sindelarova, The Copernicus Atmosphere Monitoring Service global and regional emissions, Copernicus Atmosphere Monitoring Service report, <https://doi.org/10.24380/d0bn-kx16>, 2019.

Grell, G., Freitas, S. R., Stuefer, M., and Fast, J.: Inclusion of biomass burning in WRF-Chem: impact of wildfires on weather forecasts, *Atmos. Chem. Phys.*, 11, 5289–5303, <https://doi.org/10.5194/acp-11-5289-2011>, 2011.

875

Griffin, D., McLinden, C. A., Dammers, E., Adams, C., Stockwell, C. E., Warneke, C., Bourgeois, I., Peischl, J., Ryerson, T. B., Zarzana, K. J., Rowe, J. P., Volkamer, R., Knute, C., Kille, N., Koenig, T. K., Lee, C. F., Rollins, D., Rickly, P. S., Chen, J., Fehr, L., Bourassa, A., Degenstein, D., Hayden, K., Mihele, C., Wren, S. N., Liggio, J., Akingunola, A., and Makar, P.: Biomass burning nitrogen dioxide emissions derived from space with TROPOMI: methodology and validation, *Atmos. Meas. Tech.*, 14, 7929–7957, <https://doi.org/10.5194/amt-14-7929-2021>, 2021.

880

Harmens, H., Hayes, F., Sharps, K., Radbourne, A., and Mills, G.: Can Reduced Irrigation Mitigate Ozone Impacts on an Ozone-Sensitive African Wheat Variety? *Plants*, 8, 220, <https://doi.org/10.3390/plants8070220>, 2019.

885 Holt, J., Selin, N. E., and Solomon, S.: Changes in Inorganic Fine Particulate Matter Sensitivities to Precursors Due to Large-Scale US Emissions Reductions, *Environ. Sci. Technol.*, 49, 4834–4841, <https://doi.org/10.1021/acs.est.5b00008>, 2015.

890 Horn, K. J., Thomas, R. Q., Clark, C. M., Pardo, L. H., Fenn, M. E., Lawrence, G. B., Perakis, S. S., Smithwick, E. A. H., Baldwin, D., Braun, S., Nordin, A., Perry, C. H., Phelan, J. N., Schaberg, P. G., St. Clair, S. B., Warby, R., and Watmough,

S.: Growth and survival relationships of 71 tree species with nitrogen and sulfur deposition across the conterminous U.S., *PLoS ONE*, 13, e0205296, <https://doi.org/10.1371/journal.pone.0205296>, 2018.

895 Huang, M., Bowman, K. W., Carmichael, G. R., Pierce, R. B., Worden, H. M., Luo, M., Cooper, O. R., Pollack, I. B., Ryerson, T. B., and Brown, S. S.: Impact of Southern California anthropogenic emissions on ozone pollution in the mountain states: Model analysis and observational evidence from space, *J. Geophys. Res. Atmos.*, 118, 12,784–12,803, <https://doi.org/10.1002/2013JD020205>, 2013.

900 Huang, M., Carmichael, G. R., Pierce, R. B., Jo, D. S., Park, R. J., Flemming, J., Emmons, L. K., Bowman, K. W., Henze, D. K., Davila, Y., Sudo, K., Jonson, J. E., Tronstad Lund, M., Janssens-Maenhout, G., Dentener, F. J., Keating, T. J., Oetjen, H., and Payne, V. H.: Impact of intercontinental pollution transport on North American ozone air pollution: an HTAP phase 2 multi-model study, *Atmos. Chem. Phys.*, 17, 5721–5750, <https://doi.org/10.5194/acp-17-5721-2017>, 2017a.

905 Huang, M., Carmichael, G. R., Crawford, J. H., Wisthaler, A., Zhan, X., Hain, C. R., Lee, P., and Guenther, A. B.: Biogenic isoprene emissions driven by regional weather predictions using different initialization methods: case studies during the SEAC⁴RS and DISCOVER-AQ airborne campaigns, *Geosci. Model Dev.*, 10, 3085–3104, <https://doi.org/10.5194/gmd-10-3085-2017>, 2017b.

910 Huang, M., Crawford, J. H., Carmichael, G. R., Santanello, J. A., Kumar, S. V., Stauffer, R. M., Thompson, A. M., Weinheimer, A.J., and Park, J. D.: Impact of aerosols from urban and shipping emission sources on terrestrial carbon uptake and evapotranspiration: A case study in east Asia, *J. Geophys. Res. Atmos.*, 125, e2019JD030818, <https://doi.org/10.1029/2019JD030818>, 2020.

915 Huang, M., Crawford, J. H., DiGangi, J. P., Carmichael, G. R., Bowman, K. W., Kumar, S. V., and Zhan, X.: Satellite soil moisture data assimilation impacts on modeling weather variables and ozone in the southeastern US – Part 1: An overview, *Atmos. Chem. Phys.*, 21, 11013–11040, <https://doi.org/10.5194/acp-21-11013-2021>, 2021.

920 Huang, M., Crawford, J. H., Carmichael, G. R., Bowman, K. W., Kumar, S. V., and Sweeney, C.: Satellite soil moisture data assimilation impacts on modeling weather variables and ozone in the southeastern US – Part 2: Sensitivity to dry-deposition parameterizations, *Atmos. Chem. Phys.*, 22, 7461–7487, <https://doi.org/10.5194/acp-22-7461-2022>, 2022.

Hudman, R. C., Moore, N. E., Mebust, A. K., Martin, R. V., Russell, A. R., Valin, L. C., and Cohen, R. C.: Steps towards a mechanistic model of global soil nitric oxide emissions: implementation and space based-constraints, *Atmos. Chem. Phys.*, 12, 7779–7795, <https://doi.org/10.5194/acp-12-7779-2012>, 2012.

- Huffman, G. J., Stocker, E. F., Bolvin, D. T., Nelkin, E. J., and Tan, J.: GPM IMERG Final Precipitation L3 1 day 0.1 degree \times 0.1 degree, Version 7, Goddard Earth Sciences Data and Information Services Center (GES DISC) [data set], Greenbelt, Maryland, USA, <https://doi.org/10.5067/GPM/IMERGDF/DAY/07>, 2023.
- 930 Ibebuchi, C. C., Lee, C. C., Silva, A., and Sheridan, S. C.: Evaluating apparent temperature in the contiguous United States from four reanalysis products using Artificial Neural Networks, *J. Geophys. Res.-Machine Learning and Computation*, 1, e2023JH000102, <https://doi.org/10.1029/2023JH000102>, 2024.
- Janz, S.: Long Island Sound Tropospheric Ozone Study GCAS and GeoTASO measurements of NO₂ and CH₂O, Version R1, NASA Langley Research Center Airborne Science Data for Atmospheric Composition [data set], Hampton, Virginia, USA, available at: <https://www-air.larc.nasa.gov/missions/listos/index.html> (last access: 6 February 2024), 2020.
- 935 Jia, Y., Yu, G., Gao, Y., He, N., Wang, Q., Jiao, C., and Zuo, Y.: Global inorganic nitrogen dry deposition inferred from ground- and space-based measurements, *Sci. Rep.*, 6, 19810, <https://doi.org/10.1038/srep19810>, 2016.
- 940 Jiang, X., Guenther, A., Potosnak, M., Geron, C., Seco, R., Karl, T., Kim, S., Gu, L., and Pallardy, S.: Isoprene emission response to drought and the impact on global atmospheric chemistry, *Atmos. Environ.*, 183, 69–83, <https://doi.org/10.1016/j.atmosenv.2018.01.026>, 2018.
- 945 Jin, X., Fiore, A. M., Murray, L. T., Valin, L. C., Lamsal, L. N., Duncan, B., Boersma, K. F., De Smedt, I., Abad, G. G., Chance, K., and Tonnesen, G. S.: Evaluating a Space-Based Indicator of Surface Ozone-NO_x-VOC Sensitivity Over Midlatitude Source Regions and Application to Decadal Trends, *J. Geophys. Res.-Atmos.*, 122, 10439–10461, <https://doi.org/10.1002/2017JD026720>, 2017.
- 950 Judd, L. M., Al-Saadi, J. A., Szykman, J. J., Valin, L. C., Janz, S. J., Kowalewski, M. G., Eskes, H. J., Veeffkind, J. P., Cede, A., Mueller, M., Gebetsberger, M., Swap, R., Pierce, R. B., Nowlan, C. R., Abad, G. G., Nehrir, A., and Williams, D.: Evaluating Sentinel-5P TROPOMI tropospheric NO₂ column densities with airborne and Pandora spectrometers near New York City and Long Island Sound, *Atmos. Meas. Tech.*, 13, 6113–6140, <https://doi.org/10.5194/amt-13-6113-2020>, 2020.
- 955 Karion, A., Callahan, W., Stock, M., Prinzivalli, S., Verhulst, K. R., Kim, J., Salameh, P. K., Lopez-Coto, I., and Whetstone, J.: Greenhouse gas observations from the Northeast Corridor tower network, *Earth Syst. Sci. Data*, 12, 699–717, <https://doi.org/10.5194/essd-12-699-2020>, 2020.

- 960 Keller, C. A., Evans, M. J., Knowland, K. E., Hasenkopf, C. A., Modekurty, S., Lucchesi, R. A., Oda, T., Franca, B. B.,
Mandarino, F. C., Díaz Suárez, M. V., Ryan, R. G., Fakes, L. H., and Pawson, S.: Global impact of COVID-19 restrictions
on the surface concentrations of nitrogen dioxide and ozone, *Atmos. Chem. Phys.*, 21, 3555–3592,
<https://doi.org/10.5194/acp-21-3555-2021>, 2021.
- 965 Koplitz, S. N., Nolte, C. G., Sabo, R. D., Clark, C. M., Horn, K. J., Thomas, R. Q., and Newcomer-Johnson, T. A.: The
contribution of wildland fire emissions to deposition in the US: Implications for tree growth and survival in the Northwest,
Environ. Res. Lett., 16, 024028, <https://doi.org/10.1088/1748-9326/abd26e>, 2021.
- 970 Koplitz, S., Simon, H., Henderson, B., Liljegren, J., Tonnesen, G., Whitehill, A., and Wells, B.: Changes in Ozone Chemical
Sensitivity in the United States from 2007 to 2016, *ACS Environ. Au*, 2, 206–222,
<https://doi.org/10.1021/acsenvironau.1c00029>, 2022.
- 975 Kumar, S. V., Reichle, R. H., Koster, R. D., Crow, W. T., and Peters-Lidard, C. D.: Role of subsurface physics in the
assimilation of surface soil moisture observations, *J. Hydrometeorol.*, 10, 1534–1547,
<https://doi.org/10.1175/2009JHM1134.1>, 2009.
- Lapina, K., Henze, D. K., Milford, J. B., Huang, M., Lin, M., Fiore, A. M., Carmichael, G., Pfister, G. G., and Bowman, K.:
Assessment of source contributions to seasonal vegetative exposure to ozone in the U.S., *J. Geophys. Res.-Atmos.*, 119,
324–340, <https://doi.org/10.1002/2013JD020905>, 2014.
- 980 Li, C., Martin, R. V., Cohen, R. C., Bindle, L., Zhang, D., Chatterjee, D., Weng, H., and Lin, J.: Variable effects of spatial
resolution on modeling of nitrogen oxides, *Atmos. Chem. Phys.*, 23, 3031–3049, <https://doi.org/10.5194/acp-23-3031-2023>,
2023.
- 985 Li, J., Mahalov, A., and Hyde, P.: Simulating the impacts of chronic ozone exposure on plant conductance and
photosynthesis, and on the regional hydroclimate using WRF/Chem, *Environ. Res. Lett.*, 11, 114017,
<https://doi.org/10.1088/1748-9326/11/11/114017>, 2016.
- 990 Li, Y., Schichtel, B. A., Walker, J. T., Schwede, D. B., Chen, X., Lehmann, C. M. B., Puchalski, M. A., Gay, D. A., and
Collett Jr., J. L.: Increasing importance of deposition of reduced nitrogen in the United States, *Proc. Natl. Acad. Sci. USA*,
113, 5874–5879, <https://doi.org/10.1073/pnas.1525736113>, 2016.

- Lin, M., Horowitz, L. W., Payton, R., Fiore, A. M., and Tonnesen, G.: US surface ozone trends and extremes from 1980 to 2014: quantifying the roles of rising Asian emissions, domestic controls, wildfires, and climate, *Atmos. Chem. Phys.*, 17, 2943–2970, <https://doi.org/10.5194/acp-17-2943-2017>, 2017.
- 995
- Liu, L., Zhang, X., Xu, W., Liu, X., Wei, J., Wang, Z., and Yang, Y.: Global estimates of dry ammonia deposition inferred from space-measurements, *Sci. Total Environ.*, 730, 139189, <https://doi.org/10.1016/j.scitotenv.2020.139189>, 2020a.
- Liu, L., Zhang, X., Xu, W., Liu, X., Lu, X., Wei, J., Li, Y., Yang, Y., Wang, Z., and Wong, A. Y. H.: Reviewing global estimates of surface reactive nitrogen concentration and deposition using satellite retrievals, *Atmos. Chem. Phys.*, 20, 8641–8658, <https://doi.org/10.5194/acp-20-8641-2020>, 2020b.
- 1000
- Liu, J., Clark, L. P., Bechle, M., Hajat, A., Kim, S.-Y., Robinson, A., Sheppard, Lianne, Szpiro, A. A., and Marshall, J. D.: Disparities in air pollution exposure in the United States by race-ethnicity and income, 1990–2010, *Environ. Health Perspect.*, 129, 127005, <https://doi.org/10.1289/EHP8584>, 2021.
- 1005
- Lombardozzi, D., Levis, S., Bonan, G., Hess, P. G., and Sparks, J. P.: The Influence of Chronic Ozone Exposure on Global Carbon and Water Cycles, *J. Climate*, 28, 292–305, <https://doi.org/10.1175/JCLI-D-14-00223.1>, 2015.
- Lorente, A., Boersma, K. F., Yu, H., Dörner, S., Hilboll, A., Richter, A., Liu, M., Lamsal, L. N., Barkley, M., De Smedt, I., Van Roozendaal, M., Wang, Y., Wagner, T., Beirle, S., Lin, J.-T., Krotkov, N., Stammes, P., Wang, P., Eskes, H. J., and Krol, M.: Structural uncertainty in air mass factor calculation for NO₂ and HCHO satellite retrievals, *Atmos. Meas. Tech.*, 10, 759–782, <https://doi.org/10.5194/amt-10-759-2017>, 2017.
- 1010
- Massad, R.-S., Nemitz, E., and Sutton, M. A.: Review and parameterisation of bi-directional ammonia exchange between vegetation and the atmosphere, *Atmos. Chem. Phys.*, 10, 10359–10386, <https://doi.org/10.5194/acp-10-10359-2010>, 2010.
- 1015
- Mills, G., Sharps, K., Simpson, D., Pleijel, H., Broberg, M., Uddling, J., Jaramillo, F., Davies, W. J., Dentener, F., van den Berg, M., Agrawal, M., Agrawal, S. B., Ainsworth, E. A., Buker, P., Emberson, L., Feng, Z., Harmens, H., Hayes, F., Kopbayashi, K., Paoletti, E., and Van Dingenen, R.: Ozone pollution will compromise efforts to increase global wheat production, *Global Change Biol.*, 24, 3560–3574, <https://doi.org/10.1111/gcb.14157>, 2018.
- 1020
- Miyazaki, K., Neu, J. L., Osterman, G., and Bowman, K.: Changes in US background ozone associated with the 2011 turnaround in Chinese NO_x emissions, *Environ. Res. Commun.*, 4, 045003, <https://doi.org/10.1088/2515-7620/ac619b>, 2022.
- 1025

- Monfreda, C., Ramankutty, N., and Foley, J. A.: Farming the planet: 2. Geographic distribution of crop areas, yields, physiological types, and net primary production in the year 2000, *Global Biogeochem. Cycles*, 22, GB1022, <https://doi.org/10.1029/2007GB002947>, 2008.
- 1030 Monks, P. S., Ravishankara, A. R., von Schneidmesser, E., and Sommariva, R.: Opinion: Papers that shaped tropospheric chemistry, *Atmos. Chem. Phys.*, 21, 12909–12948, <https://doi.org/10.5194/acp-21-12909-2021>, 2021.
- NCEP: NCEP ADP Global Surface Observational Weather Data, October 1999 – continuing, updated daily, Research Data Archive at the National Center for Atmospheric Research, Computational and Information Systems Laboratory [data set], 1035 Boulder, Colorado, USA, <https://doi.org/10.5065/4F4P-E398>, 2004.
- Nguyen, T. B., Crounse, J. D., Teng, A. P., Clair, J. M. S., Paulot, F., Wolfe, G. M., and Wennberg, P. O.: Rapid deposition of oxidized biogenic compounds to a temperate forest, *Proc. Natl. Acad. Sci. USA*, 112, E392–E401, <https://doi.org/10.1073/pnas.1418702112>, 2015.
- 1040 Niu, G. Y., Yang, Z. L., Mitchell, K. E., Chen, F., Ek, M. B., Barlage, M., Kumar, A., Manning, K., Niyogi, D., Rosero, E., Tewari, M., and Xia, Y.: The community Noah land surface model with multiparameterization options (Noah-MP): 1. Model description and evaluation with local-scale measurements, *J. Geophys. Res.-Atmos.*, 116, D12109, <https://doi.org/10.1029/2010JD015139>, 2011.
- 1045 O’Neill, P. E., Chan, S., Njoku, E. G., Jackson, T., Bindlish, R., Chaubell, J., and Colliander, A.: SMAP Enhanced L3 Radiometer Global and Polar Grid Daily 9 km EASE-Grid Soil Moisture, Version 5, NASA National Snow and Ice Data Center Distributed Active Archive Center [data set], Boulder, Colorado, USA, <https://doi.org/10.5067/4DQ54OUIJ9DL>, 2021.
- 1050 Oswald, R., Behrendt, T., Ermel, M., Wu, D., Su, H., Cheng, Y., Breuninger, C., Moravek, A., Mougin, E., Delon, C., Loubet, B., Pommerening-Röser, A., Sörgel, M., Pöschl, U., Hoffmann, T., Andreae, M. O., Meixner, F. X., and Trebs, I.: HONO emissions from soil bacteria as a major source of atmospheric reactive nitrogen, *Science*, 341, 1233–1235, <https://doi.org/10.1126/science.1242266>, 2013.
- 1055 Ott, L. E., Duncan, B. N., Thompson, A. M., Diskin, G., Fasnacht, Z., Langford, A. O., Lin, M., Molod, A. M., Nielsen, J. E., Pusede, S. E., Wargan, K., Weinheimer, A. J., and Yoshida, Y.: Frequency and impact of summertime stratospheric intrusions over Maryland during DISCOVER-AQ (2011): New evidence from NASA's GEOS-5 simulations, *J. Geophys. Res.-Atmos.*, 121, 3687–3706, <https://doi.org/10.1002/2015JD024052>, 2016.

1060

Pardo, L. H., Fenn, M.E., Goodale, C. L., Geiser, L. H., Driscoll, C. T., Allen, E. B., Baron, J. S., Bobbink, R., Bowman, W. D., Clark, C. M., Emmett, B., Gilliam, F. S., Greaver, T. L., Hall, S. J., Lilleskov, E. A., Liu, L., Lynch, J. A., Nadelhoffer, K. J., Perakis, S. S., Robin-Abbott, M. J., Stoddard, J. L., Weathers, K. C., and Dennis, R. L.: Effects of nitrogen deposition and empirical nitrogen critical loads for ecoregions of the United States, *Ecol. Appl.*, 21, 3049–3082, <https://doi.org/10.1007/s11270014-2109-4>, 2011.

1065

Pleim, J. E., Ran, L., Appel, W., Shephard, M. W., and Cady-Pereira, K.: New bidirectional ammonia flux model in an air quality model coupled with an agricultural model, *J. Adv. Model. Earth Syst.*, 11, 2934–2957, <https://doi.org/10.1029/2019MS0017282934>, 2019.

1070

Putero, D., Cristofanelli, P., Chang, K.-L., Dufour, G., Beachley, G., Couret, C., Effertz, P., Jaffe, D. A., Kubistin, D., Lynch, J., Petropavlovskikh, I., Puchalski, M., Sharac, T., Sive, B. C., Steinbacher, M., Torres, C., and Cooper, O. R.: Fingerprints of the COVID-19 economic downturn and recovery on ozone anomalies at high-elevation sites in North America and western Europe, *Atmos. Chem. Phys.*, 23, 15693–15709, <https://doi.org/10.5194/acp-23-15693-2023>, 2023.

1075

Rasool, Q. Z., Bash, J. O., and Cohan, D. S.: Mechanistic representation of soil nitrogen emissions in the Community Multiscale Air Quality (CMAQ) model v5.1, *Geosci. Model Dev.*, 12, 849–878, <https://doi.org/10.5194/gmd-12-849-2019>, 2019.

1080

Rogers, H. M., Ditto, J. C., and Gentner, D. R.: Evidence for impacts on surface-level air quality in the northeastern US from long-distance transport of smoke from North American fires during the Long Island Sound Tropospheric Ozone Study (LISTOS) 2018, *Atmos. Chem. Phys.*, 20, 671–682, <https://doi.org/10.5194/acp-20-671-2020>, 2020.

1085

Rubin, H. J., Fu, J. S., Dentener, F., Li, R., Huang, K., and Fu, H.: Global nitrogen and sulfur deposition mapping using a measurement–model fusion approach, *Atmos. Chem. Phys.*, 23, 7091–7102, <https://doi.org/10.5194/acp-23-7091-2023>, 2023.

1090

Ryu, Y.-H. and Min, S.-K.: Improving wet and dry deposition of aerosols in WRF-Chem: Updates to below-cloud scavenging and coarse-particle dry deposition, *J. Adv. Model. Earth Syst.*, 14, e2021MS002792, <https://doi.org/10.1029/2021MS002792>, 2022.

- Paulot, F., Jacob, D. J., and Henze, D. K.: Sources and Processes Contributing to Nitrogen Deposition: An Adjoint Model Analysis Applied to Biodiversity Hotspots Worldwide, *Environ. Sci. Technol.*, 47, 3226–3233, <https://doi.org/10.1021/es3027727>, 2013.
- 1095 Paulot, F., Malyshev, S., Nguyen, T., Crouse, J. D., Shevliakova, E., and Horowitz, L. W.: Representing sub-grid scale variations in nitrogen deposition associated with land use in a global Earth system model: implications for present and future nitrogen deposition fluxes over North America, *Atmos. Chem. Phys.*, 18, 17963–17978, <https://doi.org/10.5194/acp-18-17963-2018>, 2018.
- 1100 Sadiq, M., Tai, A. P. K., Lombardozzi, D., and Val Martin, M.: Effects of ozone–vegetation coupling on surface ozone air quality via biogeochemical and meteorological feedbacks, *Atmos. Chem. Phys.*, 17, 3055–3066, <https://doi.org/10.5194/acp-17-3055-2017>, 2017.
- 1105 Salmon, J. M., Friedl, M. A., Frohling, S., Wisser, D., and Douglas, E. M.: Global rain-fed, irrigated, and paddy croplands: A new high resolution map derived from remote sensing, crop inventories and climate data, *Int. J. Appl. Earth Obs.*, 38, 321–334, <https://doi.org/10.1016/j.jag.2015.01.014>, 2015.
- Schwede, D. B. and Lear, G. G.: A novel hybrid approach for estimating total deposition in the United States, *Atmos. Environ.*, 92, 207–220, <http://dx.doi.org/10.1016/j.atmosenv.2014.04.008>, 2014.
- 1110 Seinfeld, J. H. and Pandis, S. N.: *Atmospheric chemistry and physics: from air pollution to climate change*, Third edition, John Wiley & Sons, Inc., Hoboken, New Jersey, 2016.
- 1115 Seneviratne, S. I., Corti, T., Davin, E. L., Hirschi, M., Jaeger, E. B., Lehner, I., Orlowsky, B., and Teuling, A. J.: Investigating soil moisture–climate interactions in a changing climate: A review, *Earth-Sci. Rev.*, 99, 125–161, <https://doi.org/10.1016/j.earscirev.2010.02.004>, 2010.
- 1120 Simkin, S. M., Allen, E. B., Bowman, W. D., Clark, C. M., Belnap, J., Brooks, M. L., Cade, B. S., Collins, S. L., Geiser, L. H., Gilliam, F. S., Jovan, S. E., Pardo, L. H., Schulz, B. K., Stevens, C. J., Suding, K. N., Throop, H. L., and Waller, D. M.: Conditional vulnerability of plant diversity to atmospheric nitrogen deposition across the United States, *Proc. Natl. Acad. Sci. USA*, 113, 4086–4091, <https://doi.org/10.1073/pnas.1515241113>, 2016.
- 1125 Simon, H., Reff, A., Wells, B., Xing, J., and Frank, N.: Ozone Trends Across the United States over a Period of Decreasing NO_x and VOC Emissions, *Environ. Sci. Technol.*, 49, 186–195, <https://doi.org/10.1021/es504514z>, 2015.

- Simpson, D., Arneth, A., Mills, G., Solberg, S., and Uddling, J.: Ozone—the persistent menace: interactions with the N cycle and climate change, *Curr. Opin. Environ. Sustain.*, 919, 9–10, <https://doi.org/10.1016/j.cosust.2014.07.008>, 2014.
- 1130 Simpson, D. and Darras, S.: Global soil NO emissions for Atmospheric Chemical Transport Modelling: CAMS-GLOB-SOIL v2.2, *Earth Syst. Sci. Data Discuss.* [preprint], <https://doi.org/10.5194/essd-2021-221>, 2021.
- Soulie, A., Granier, C., Darras, S., Zilbermann, N., Doumbia, T., Guevara, M., Jalkanen, J.-P., Keita, S., Lioussé, C., Crippa, M., Guizzardi, D., Hoesly, R., and Smith, S. J.: Global anthropogenic emissions (CAMS-GLOB-ANT) for the Copernicus
1135 Atmosphere Monitoring Service simulations of air quality forecasts and reanalyses, *Earth Syst. Sci. Data*, 16, 2261–2279, <https://doi.org/10.5194/essd-16-2261-2024>, 2024.
- Souri, A. H., Johnson, M. S., Wolfe, G. M., Crawford, J. H., Fried, A., Wisthaler, A., Brune, W. H., Blake, D. R., Weinheimer, A. J., Verhoelst, T., Compornolle, S., Pinardi, G., Vigouroux, C., Langerock, B., Choi, S., Lamsal, L., Zhu, L.,
1140 Sun, S., Cohen, R. C., Min, K.-E., Cho, C., Philip, S., Liu, X., and Chance, K.: Characterization of errors in satellite-based HCHO/NO₂ tropospheric column ratios with respect to chemistry, column-to-PBL translation, spatial representation, and retrieval uncertainties, *Atmos. Chem. Phys.*, 23, 1963–1986, <https://doi.org/10.5194/acp-23-1963-2023>, 2023.
- Steinbrecht, W., Kubistin, D., Plass-Dülmer, C., Davies, J., Tarasick, D. W., von der Gathen, P., Deckelmann, H., Jepsen,
1145 N., Kivi, R., Lyall, N., Palm, M., Notholt, J., Kois, B., Oelsner, P., Allaart, M., Piters, A., Gill, M., Van Malderen, R., Delcloo, A. W., Sussmann, R., Mahieu, E., Servais, C., Romanens, G., Stübi, R., Ancellet, G., Godin-Beekmann, S., Yamanouchi, S., Strong, K., Johnson, B., Cullis, P., Petropavlovskikh, I., Hannigan, J. W., Hernandez, J.-L., Rodriguez, A. D., Nakano, T., Chouza, F., Leblanc, T., Torres, C., Garcia, O., Röhlings, A. N., Schneider, M., Blumenstock, T., Tully, M., Paton-Walsh, C., Jones, N., Querel, R., Strahan, S., Stauffer, R. M., Thompson, A. M., Inness, A., Engelen, R., Chang, K.-
1150 L., and Cooper, O. R.: COVID-19 Crisis Reduces Free Tropospheric Ozone Across the Northern Hemisphere, *Geophys. Res. Lett.*, 48, e2020GL091987, <https://doi.org/10.1029/2020GL091987>, 2021.
- Steinkamp, J. and Lawrence, M. G.: Improvement and evaluation of simulated global biogenic soil NO emissions in an AC-GCM, *Atmos. Chem. Phys.*, 11, 6063–6082, <https://doi.org/10.5194/acp-11-6063-2011>, 2011.
1155
- Sun, S., Tai, A. P. K., Yung, D. H. Y., Wong, A. Y. H., Ducker, J. A., and Holmes, C. D.: Influence of plant ecophysiology on ozone dry deposition: comparing between multiplicative and photosynthesis-based dry deposition schemes and their responses to rising CO₂ level, *Biogeosciences*, 19, 1753–1776, <https://doi.org/10.5194/bg-19-1753-2022>, 2022.

- 1160 Tao, M., Fiore, A. M., Jin, X., Schiferl, L. D., Commane, R., Judd, L. M., Janz, S., Sullivan, J. T., Miller, P. J., Karambelas, A., Davis, S., Tzortziou, M., Valin, L., Whitehill, A., Civerolo, K., and Tian, Y.: Investigating Changes in Ozone Formation Chemistry during Summertime Pollution Events over the Northeastern United States, *Environ. Sci. Technol.*, 56, 15312–15327, <https://doi.org/10.1021/acs.est.2c02972>, 2022.
- 1165 Tan, J., Fu, J. S., Dentener, F., Sun, J., Emmons, L., Tilmes, S., Sudo, K., Flemming, J., Jonson, J. E., Gravel, S., Bian, H., Davila, Y., Henze, D. K., Lund, M. T., Kucsera, T., Takemura, T., and Keating, T.: Multi-model study of HTAP II on sulfur and nitrogen deposition, *Atmos. Chem. Phys.*, 18, 6847–6866, <https://doi.org/10.5194/acp-18-6847-2018>, 2018.
- United Nations Economic Commission for Europe: Guidance documents and other methodological materials for the
1170 implementation of the 1999 Protocol to Abate Acidification, Eutrophication and Ground-level Ozone (Gothenburg Protocol), <https://unece.org/gothenburg-protocol> (last access: 12 January 2023), 1999.
- US Environmental Protection Agency (EPA): Nonattainment Areas for Criteria Pollutants (Green Book),
<https://www.epa.gov/green-book>, 2023.
- 1175 US EPA: AQS Hourly Ozone Data, US EPA Office of Air Quality Planning and Standards/Outreach and Information Division/National Air Data Group [data set], Research Triangle Park, North Carolina, USA, available at: https://aq5.epa.gov/aqsweb/airdata/download_files.html (last access: 1 October 2024), 2024.
- 1180 US Global Change Research Program: Fifth National Climate Assessment, Crimmins, A. R., Avery, C. W., Easterling, D. R., Kunkel, K. E., Stewart, B. C., and Maycock, T. K. Eds., US. Global Change Research Program, Washington, DC, USA, <https://doi.org/10.7930/NCA5.2023>, 2023.
- van der Velde, I. R., van der Werf, G. R., Houweling, S., Eskes, H. J., Veeffkind, J. P., Borsdorff, T., and Aben, I.: Biomass
1185 burning combustion efficiency observed from space using measurements of CO and NO₂ by the TROPOspheric Monitoring Instrument (TROPOMI), *Atmos. Chem. Phys.*, 21, 597–616, <https://doi.org/10.5194/acp-21-597-2021>, 2021.
- Veira, A., Kloster, S., Schutgens, N. A. J., and Kaiser, J. W.: Fire emission heights in the climate system – Part 2: Impact on
1190 transport, black carbon concentrations and radiation, *Atmos. Chem. Phys.*, 15, 7173–7193, <https://doi.org/10.5194/acp-15-7173-2015>, 2015.

- Vinken, G. C. M., Boersma, K. F., Maasakkers, J. D., Adon, M., and Martin, R. V.: Worldwide biogenic soil NO_x emissions inferred from OMI NO₂ observations, *Atmos. Chem. Phys.*, 14, 10363–10381, <https://doi.org/10.5194/acp-14-10363-2014>, 1195 2014.
- Walker, J. T., Beachley, G., Amos, H. M., Baron, J. S., Bash, J., Baumgardner, R., Bell, M. D., Benedict, K. B., Chen, X., Clow, D. W., Cole, A., Coughlin, J. G., Cruz, K., Daly, R. W., Decina, S. M., Elliott, E. M., Fenn, M. E., Ganzeveld, L., Gebhart, K., Isil, S. S., Kerschner, B. M., Larson, R. S., Lavery, T., Lear, G. G., Macy, T., Mast, M. A., Mishoe, K., Morris, 1200 K. H., Padgett, P. E., Pouyat, R. V., Puchalski, M., Pye, H., Rea, A. W., Rhodes, M. F., Rogers, C. M., Saylor, R., Scheffe, R., Schichtel, B. A., Schwede, D. B., Sextstone, G. A., Sive, B. C., Sosa, R., Templer, P. H., Thompson, T., Tong, D., Wetherbee, G. A., Whitlow, T. H., Wu, Z., Yu, Z., and Zhang, L.: Toward the improvement of total nitrogen deposition budgets in the United States, *Sci. Total Environ.*, 691, 1328–1352, <https://doi.org/10.1016/j.scitotenv.2019.07.058>, 2019.
- 1205 Wang, Y., Ge, C., Garcia, L. C., Jenerette, G. D., Oikawa, P. Y., and Wang, J.: Improved modelling of soil NO_x emissions in a high temperature agricultural region: role of background emissions on NO₂ trend over the US, *Environ. Res. Lett.*, 16, 084061, <https://doi.org/10.1088/1748-9326/ac16a3>, 2021.
- Wiedinmyer, C., Kimura, Y., McDonald-Buller, E. C., Emmons, L. K., Buchholz, R. R., Tang, W., Seto, K., Joseph, M. B., 1210 Barsanti, K. C., Carlton, A. G., and Yokelson, R.: The Fire Inventory from NCAR version 2.5: an updated global fire emissions model for climate and chemistry applications, *Geosci. Model Dev.*, 16, 3873–3891, <https://doi.org/10.5194/gmd-16-3873-2023>, 2023.
- Wong, J., Barth, M. C., and Noone, D.: Evaluating a lightning parameterization based on cloud-top height for mesoscale 1215 numerical model simulations, *Geosci. Model Dev.*, 6, 429–443, <https://doi.org/10.5194/gmd-6-429-2013>, 2013.
- Wu, Z., Wang, X., Chen, F., Turnipseed, A. A., Guenther, A. B., Niyogi, D., Charusombat, U., Xia, B., Munger, J. W., and Alapaty, K.: Evaluating the calculated dry deposition velocities of reactive nitrogen oxides and ozone from two community 1220 models over a temperate deciduous forest, *Atmos. Environ.*, 45, 2663–2674, <https://doi.org/10.1016/j.atmosenv.2011.02.063>, 2011.
- Yao, L., Kong, S., Nemitz, E., Vieno, M., Cheng, Y., Zheng, H., Wang, Y., Chen, N., Hu, Y., Liu, D., Zhao, T., Bai, Y., and Qi, S.: Improving below-cloud scavenging coefficients of sulfate, nitrate, and ammonium in PM_{2.5} and implications for 1225 numerical simulation and air pollution control, *J. Geophys. Res. Atmos.*, 129, e2023JD039487, <https://doi.org/10.1029/2023JD039487>, 2023.

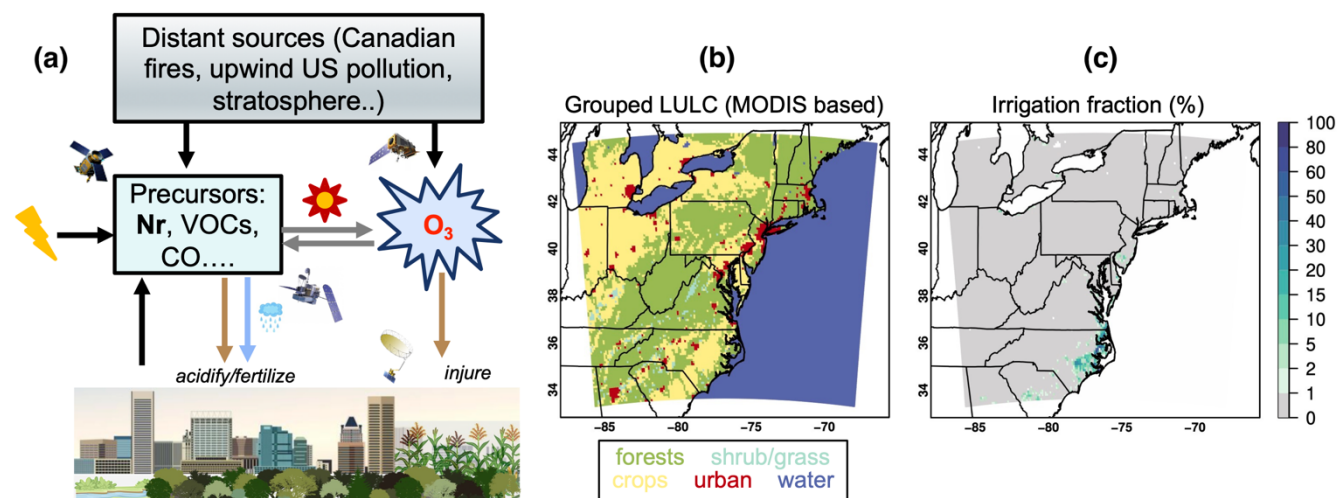
Zhang, L., Wright, L. P., and Asman, W. A. H.: Bi-directional air-surface exchange of atmospheric ammonia: A review of measurements and a development of a big-leaf model for applications in regional-scale air-quality models, *J. Geophys. Res.*, 115, D20310, <https://doi.org/10.1029/2009JD013589>, 2010.

1230

Zhu, L., Henze, D., Bash, J., Jeong, G.-R., Cady-Pereira, K., Shephard, M., Luo, M., Paulot, F., and Capps, S.: Global evaluation of ammonia bidirectional exchange and livestock diurnal variation schemes, *Atmos. Chem. Phys.*, 15, 12823–12843, <https://doi.org/10.5194/acp-15-12823-2015>, 2015.

1235 Zhu, J. and Liang, X.-Z.: Impacts of the Bermuda High on regional climate and ozone over the United States, *J. Climate*, 26, 1018–1032, <https://doi.org/10.1175/JCLI-D-12-00168.1>, 2013.

Figures



1240 **Figure 1: (a) A simplified schematic representation of Nr-O₃ relationships in the Earth systems; (b) model domain and the grid-**
dominant land use/land cover (LULC) classifications, grouped from the original 20-category International Geosphere-Biosphere
Programme-modified Moderate Resolution Imaging Spectroradiometer (MODIS) using the same criteria as in Huang et al. (2022);
and (c) irrigation fraction information required in the irrigation scheme. The grouped LULC is used for reporting potential O₃
and Nr ecosystem impacts in Section 3.2, and approximately 32%, 24%, 1%, 3%, and 40% of model grids belong to the grouped
 1245 **forests, crops, shrub/grass, urban, and water category, respectively.**

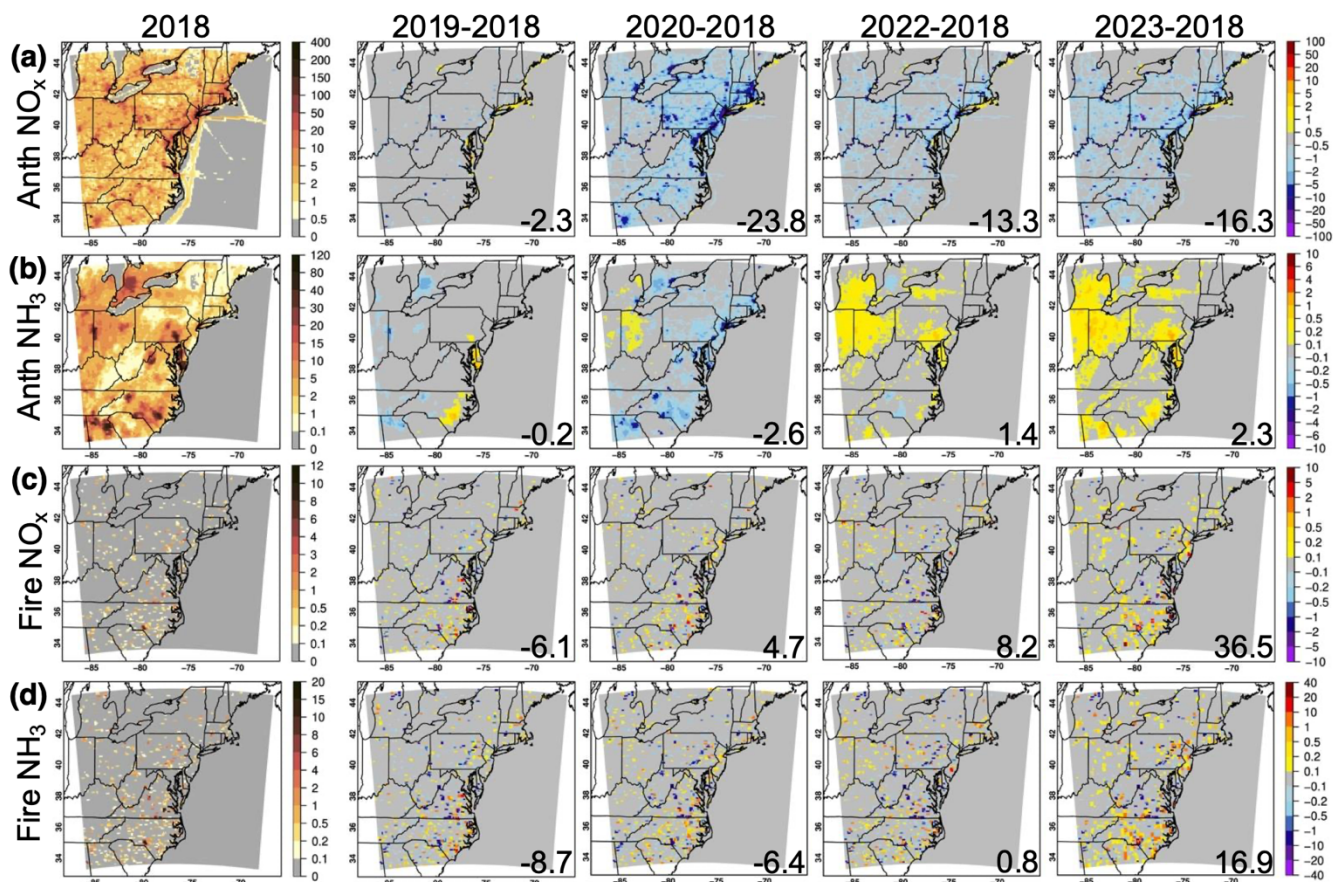


Figure 2: (a;b) Anthropogenic (Anth) and (c;d) biomass burning (fire) (a;c) NO_x and (b;d) NH_3 emissions for MJJ 2018 and the differences between MJJ of each of the following years and 2018, in $\text{mol km}^{-2} \text{h}^{-1}$. Numbers at the corners of the difference plots indicate the % changes relative to MJJ 2018.

1250

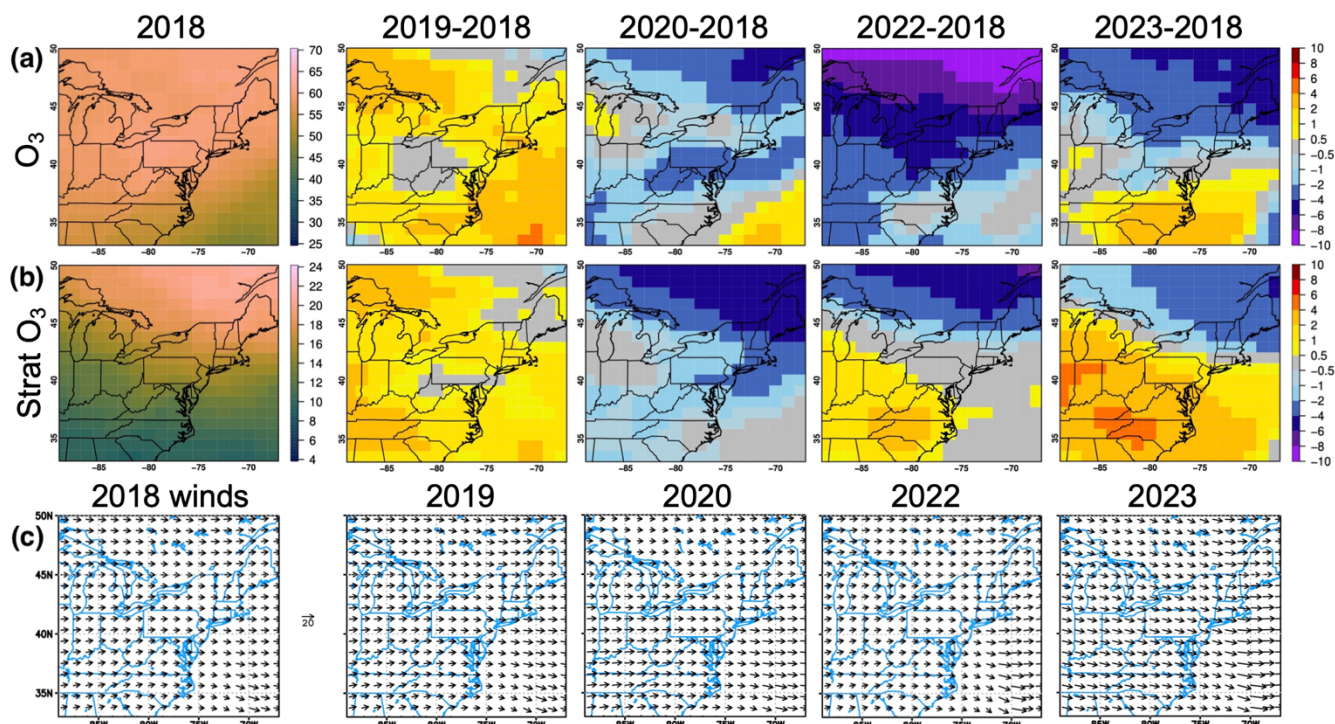


Figure 3: MJJ ~600–800 hPa (a) total and (b) stratospheric O_3 and their interannual differences in ppbv, and (c) wind fields for each year's MJJ, from WRF-Chem's chemical boundary condition models. Stratospheric O_3 impacts on the surface are indicated in Fig. S2.

1255

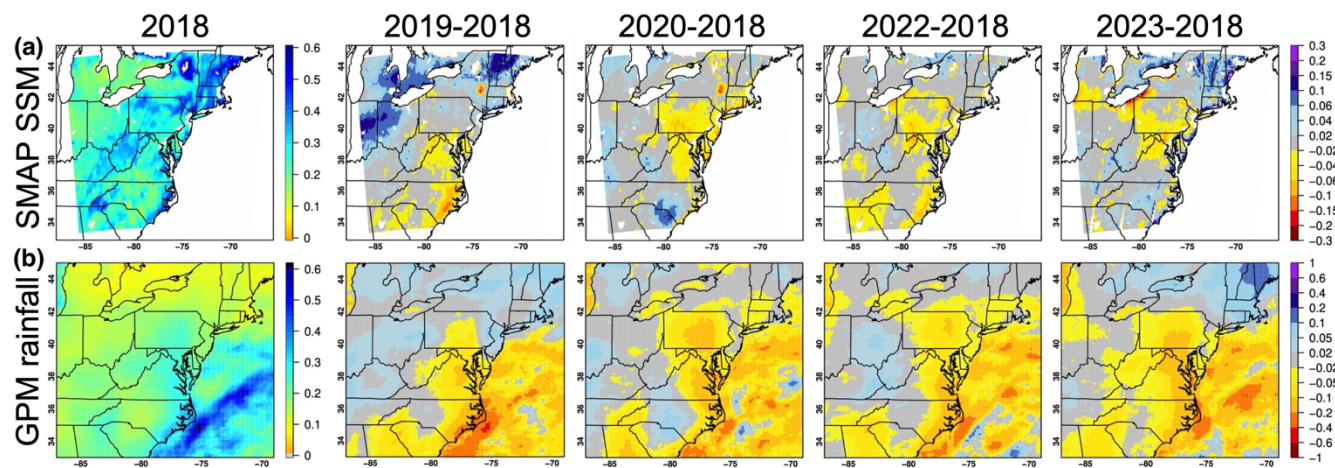
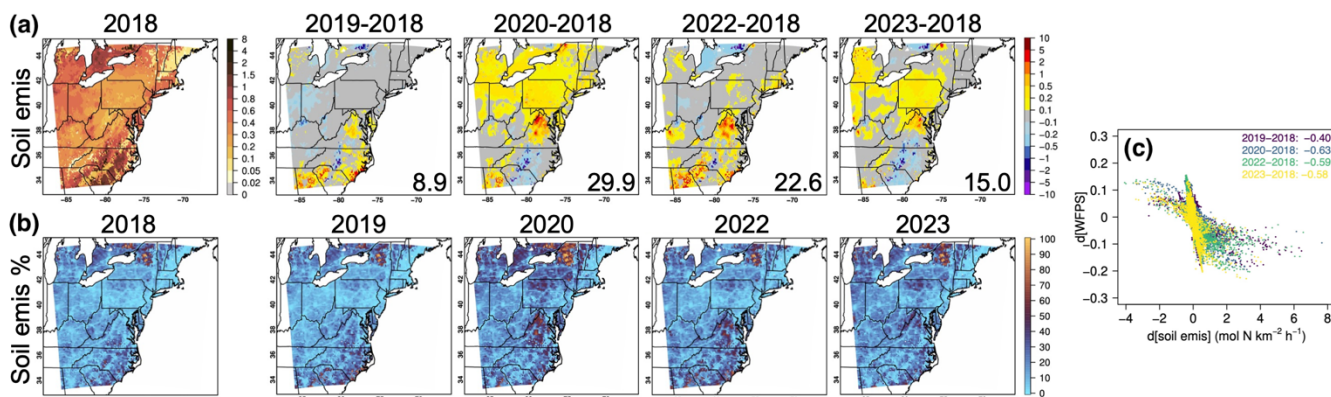
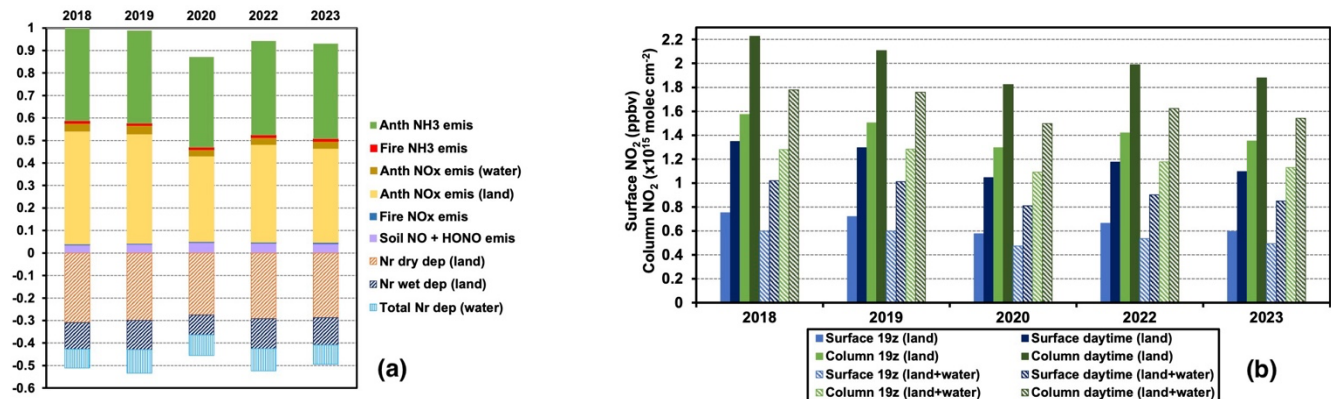


Figure 4: (a) SMAP morning-time SSM ($m^3 m^{-3}$) on WRF-Chem grids and (b) GPM/IMERG precipitation ($mm h^{-1}$) on its native grid for MJJ 2018 (left) and the differences between MJJ of each of the following years and 2018. SMAP measures the globe every 2–3 days and GPM daily global-coverage products are used for this work. SMAP data are not available during 20 June–22 July 2019 due to instrument outages; and the ESA CCI version 8.1 SM product indicates qualitatively similar MJJ 2019-2018 variability.

1260



1265 **Figure 5: (a) Modeled soil NO and HONO emissions ($\text{mol N km}^{-2} \text{h}^{-1}$) and (b) soil NO and HONO emission % contributions to total anth+fire+soil NO_y emissions. Model results are averaged for MJJ 2018, shown together with the differences between MJJ of each of the following years and 2018. Numbers at the corners of the soil emission difference plots in (a) indicate the % changes relative to MJJ 2018. The scatterplot in (c) indicates relationships between the interannual differences in water-filled pore space (WFPS, whose spatial patterns are shown in Fig. S5) and soil NO_y emissions including their correlation coefficients in the upper-right legend ($p \ll 0.01$).**



1270 **Figure 6: (a) Emission and deposition fluxes by year, scaled to MJJ 2018 total emissions; (b) Domain-wide MJJ-average surface and column NO_2 , summarized for early-afternoon (19 UTC) and daytime, and for land and all model grids. Water and land model grids are defined in Fig. 1b.**

1275

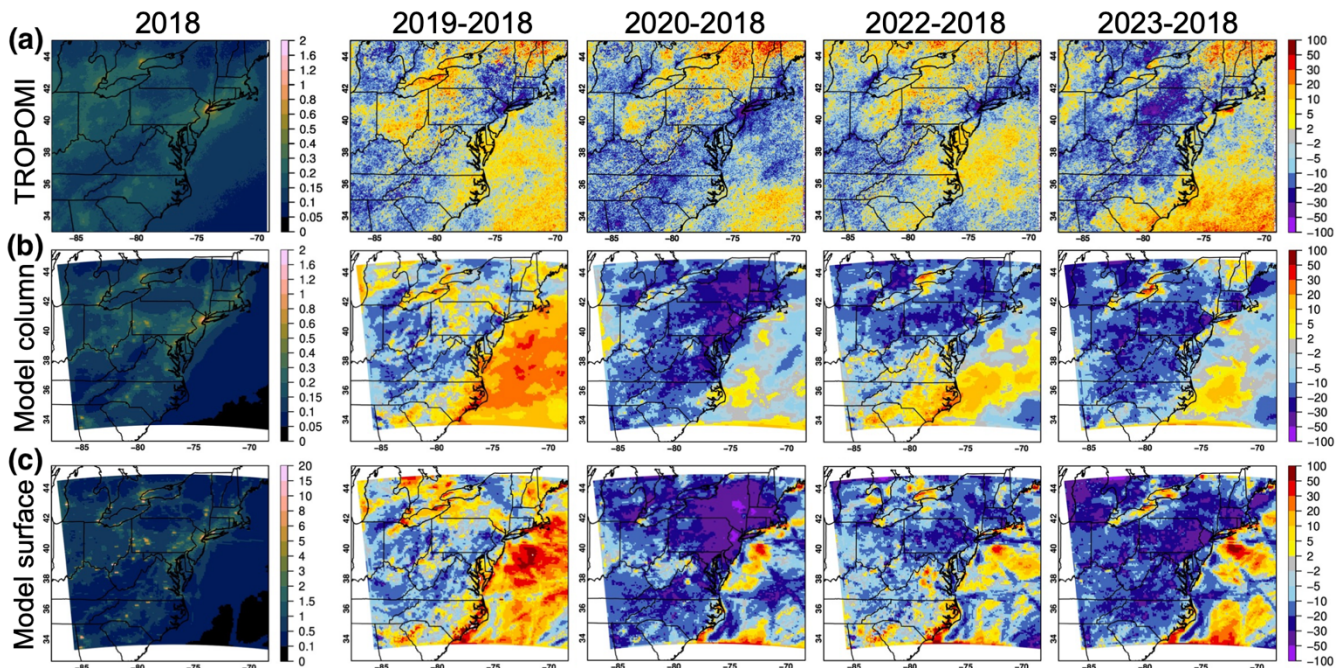


Figure 7: (a) TROPOMI and (b) WRF-Chem NO_2 columns; and (c) WRF-Chem surface NO_2 at 19 UTC. Results are averaged for MJJ 2018 (left, in $\times 10^{16}$ molec. cm^{-2} for column NO_2 and ppbv for surface NO_2) and shown together with the % differences between MJJ of each of the following years and 2018.

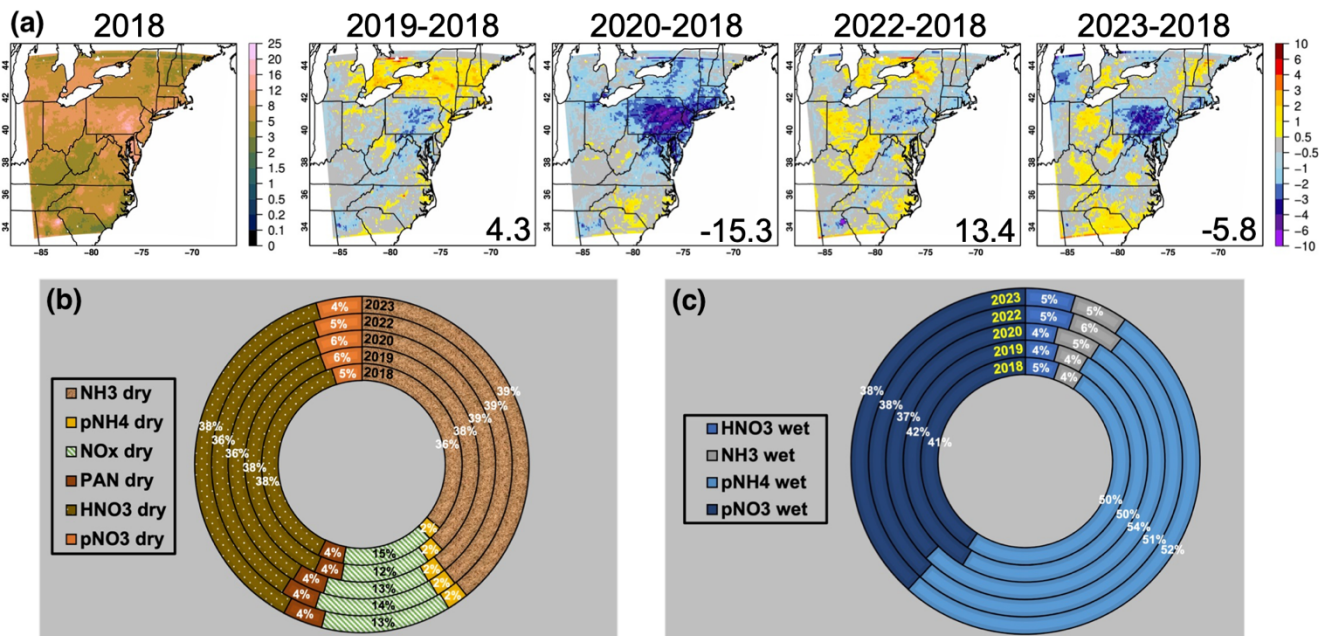
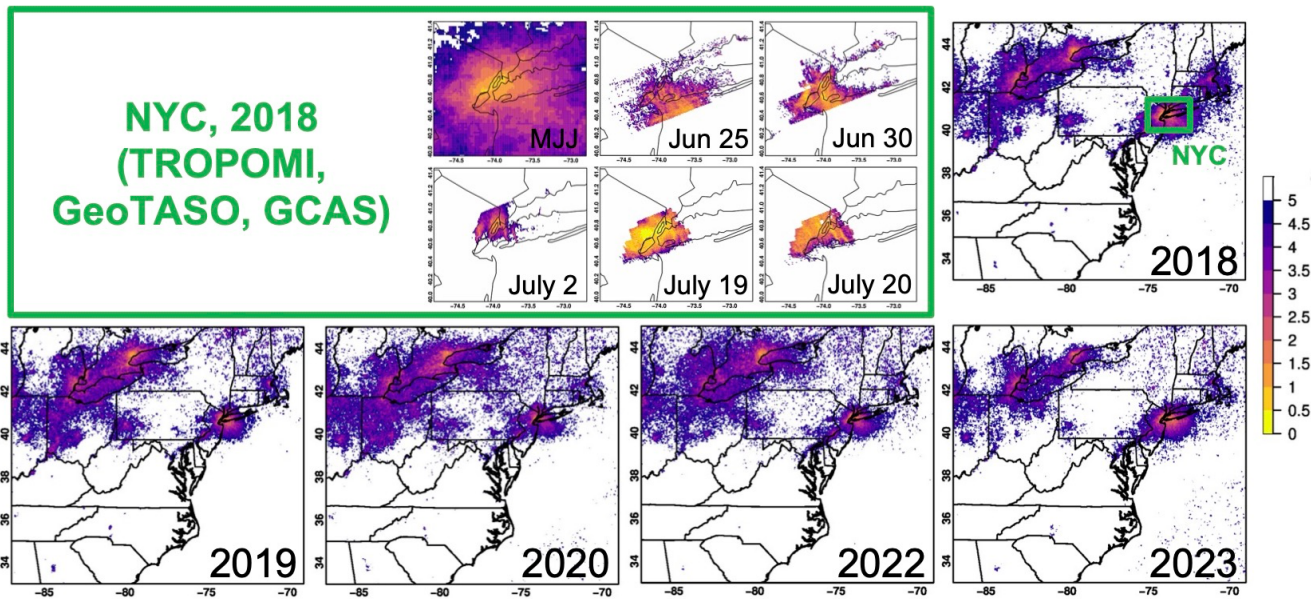
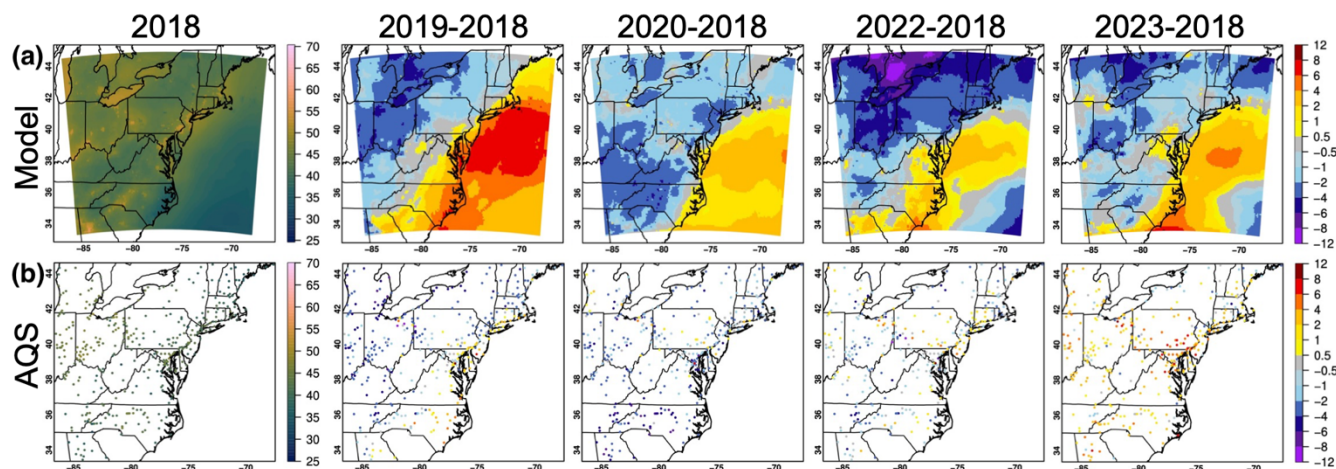


Figure 8: (a) Modeled MJJ 2018 total Nr deposition overland and differences between MJJ of each of the following years and 2018 in $\text{kgN ha}^{-1} \text{a}^{-1}$; and speciation of modeled (b) dry and (c) wet deposition fluxes by year, where prefix “p” indicates particle.



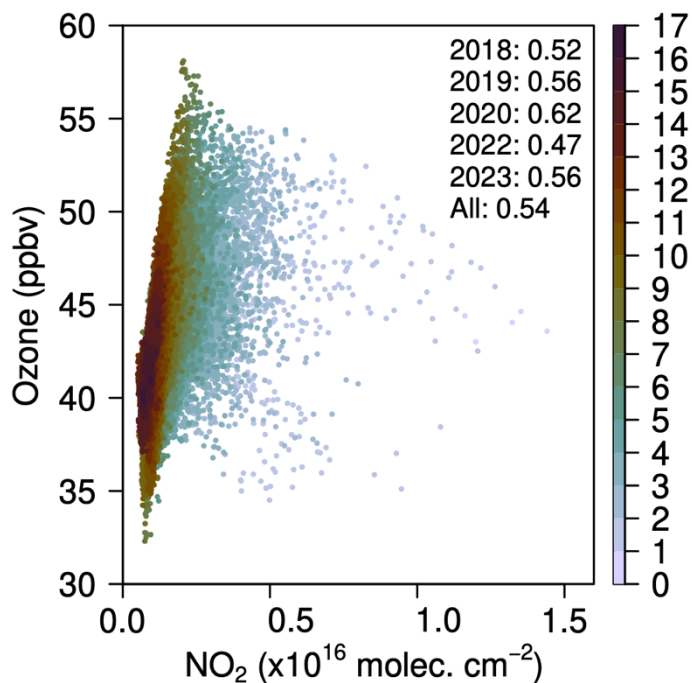
1285

Figure 9: TROPOMI (MJJ 2018–2023), GeoTASO (25 and 30 June 2018) and GCAS (2, 19 and 20 July 2018) HCHO/NO₂ ratios. GeoTASO and GCAS both took measurements over the Greater New York City (NYC) several times during the sampling days which indicate subdaily variability in HCHO, NO₂ and their ratio. Their measurements closest to 19 UTC are used here.



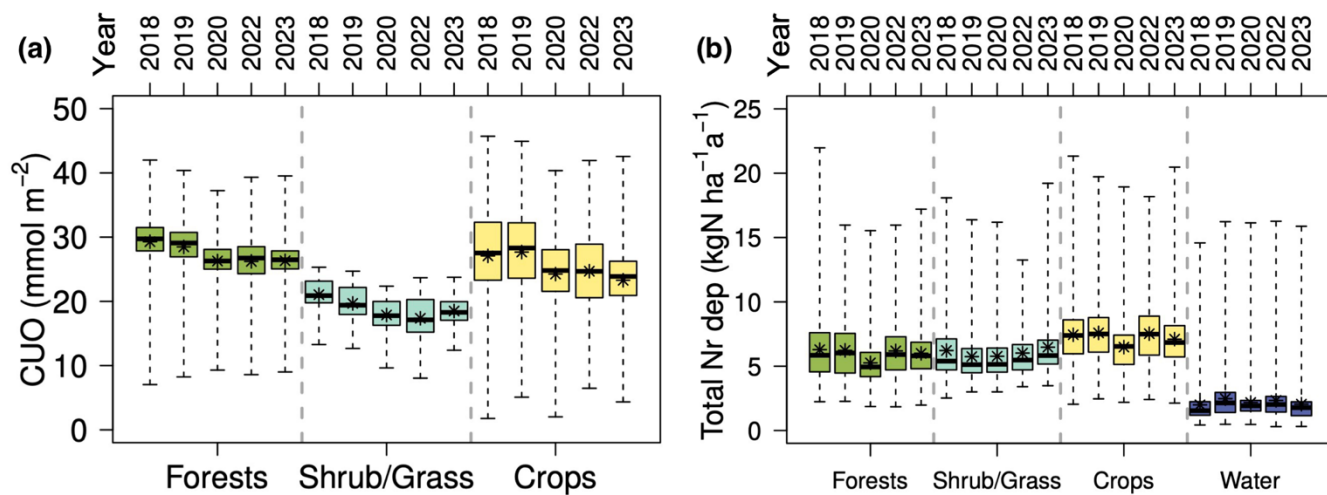
1290

Figure 10: (a) WRF-Chem modeled and (b) AQS daytime surface O₃. Results are averaged for MJJ 2018, shown together with the differences between MJJ of each of the following years and 2018, all in ppbv. Observations from the AQS sites having <10% missing data for each year were used for evaluation. Model vs. AQS RMSEs (number of grids having collocated observations) for 2018, 2019, 2020, 2022, 2023 are 5.6 (375), 6.5 (377), 5.9 (373), 4.8 (370), and 4.0 (381), respectively.



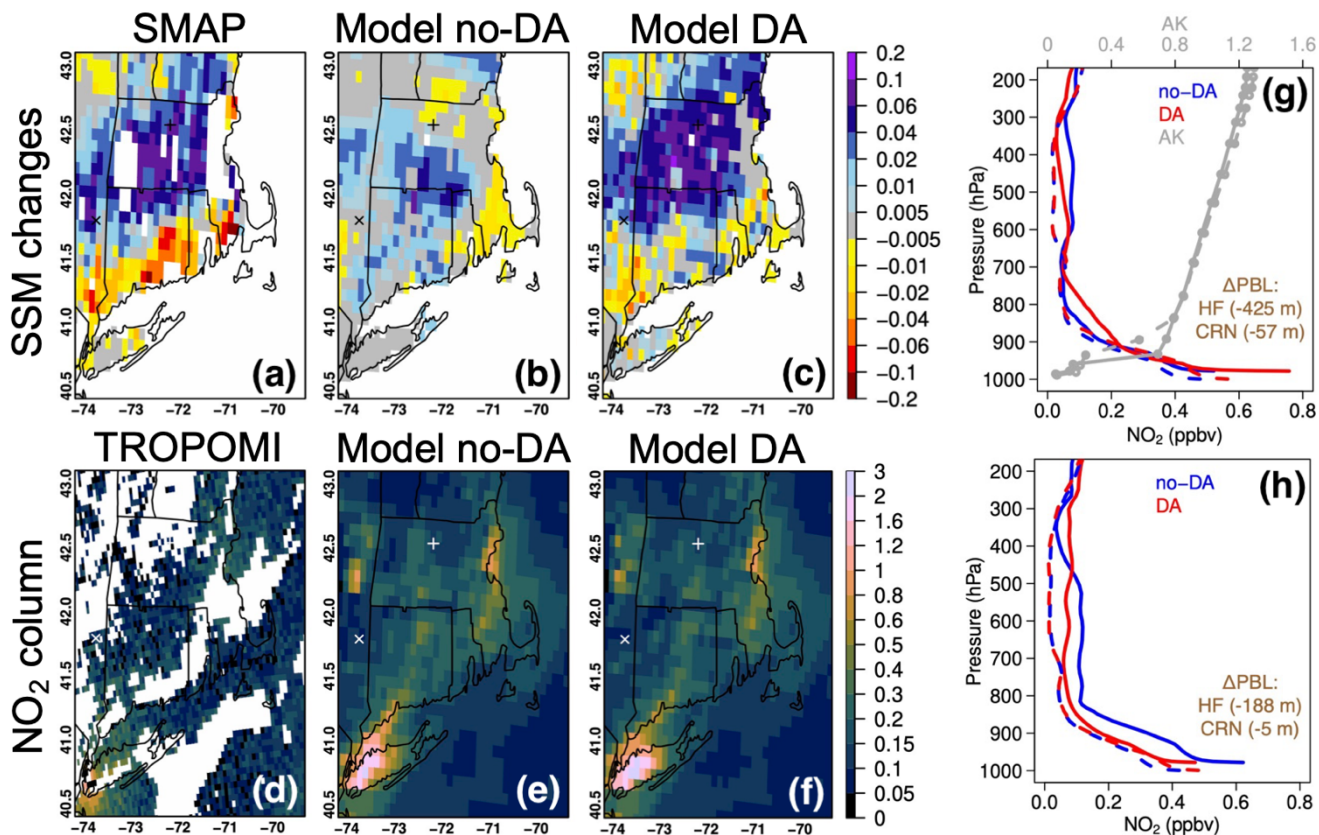
1295

Figure 11: Scatterplot indicating the relationships between WRF-Chem modeled daytime surface O₃ and 19 UTC NO₂ column during MJJ 2018–2023 for all terrestrial model grids, colored by column HCHO/NO₂ ratios. Their correlation coefficients ($p < 0.01$) are indicated in the corner legend by year.



1300

Figure 12: Box-and-Whisker plots of (a) CUO and (b) mean total Nr deposition fluxes for MJJ 2018–2023 by the grouped surface types defined in Fig. 1b.



1305

Figure 13: (a–c) 14 July–11 July SSM ($\text{m}^3 \text{m}^{-3}$) changes indicated by bias-corrected SMAP, free-running and SMAP-constrained Noah-MP results; (d–f) 14 July TROPOMI NO_2 columns ($\times 10^{16} \text{ molec. cm}^{-2}$) collected between 18–19 UTC, free-running and SMAP-constrained WRF-Chem results at 18 UTC; NO_2 vertical profiles from free-running and SMAP-constrained WRF-Chem at Harvard Forest (HF, solid line) and CRN-Millbrook (dash line) at (g) 18 UTC and (h) 19 UTC on 14 July, along with the impact of SMAP DA on modeled boundary layer height (PBL) as well as TROPOMI averaging kernels (AK) on TROPOMI’s *a priori* model grid. The white + and × signs in (a–f) denote the locations of HF and CRN-Millbrook where in situ precipitation and SSM data are also analyzed. Ground-based SSM measurements on 11 July and 14 July near SMAP overpasses are 0.170 ± 0.059 and $0.245 \pm 0.080 \text{ m}^3 \text{m}^{-3}$ at HF, and 0.067 and 0.086 at CRN-Millbrook, respectively. Precipitation and ground-based O_3 fields on 11 and 14 July are shown in Fig. S17.

1310

1315

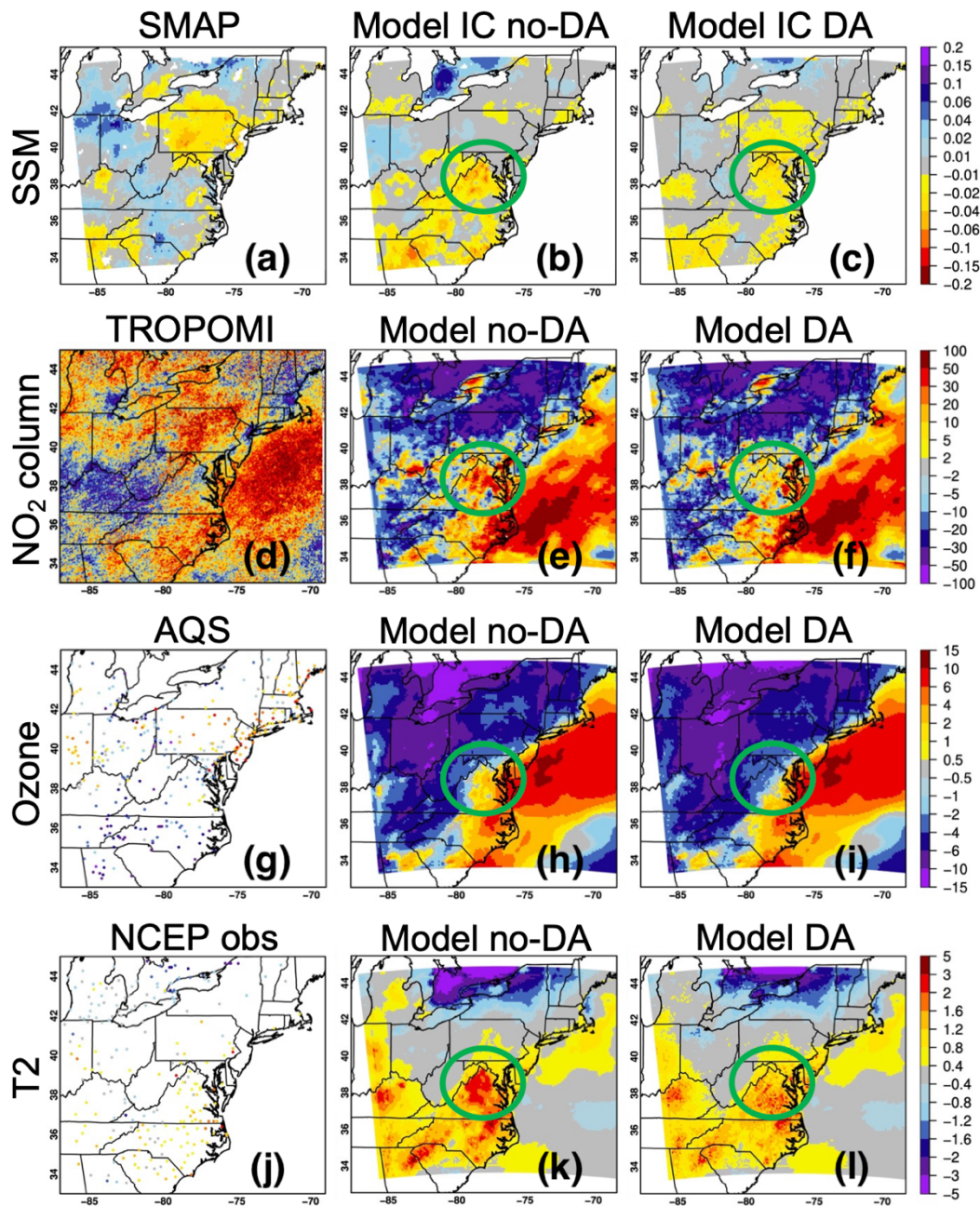
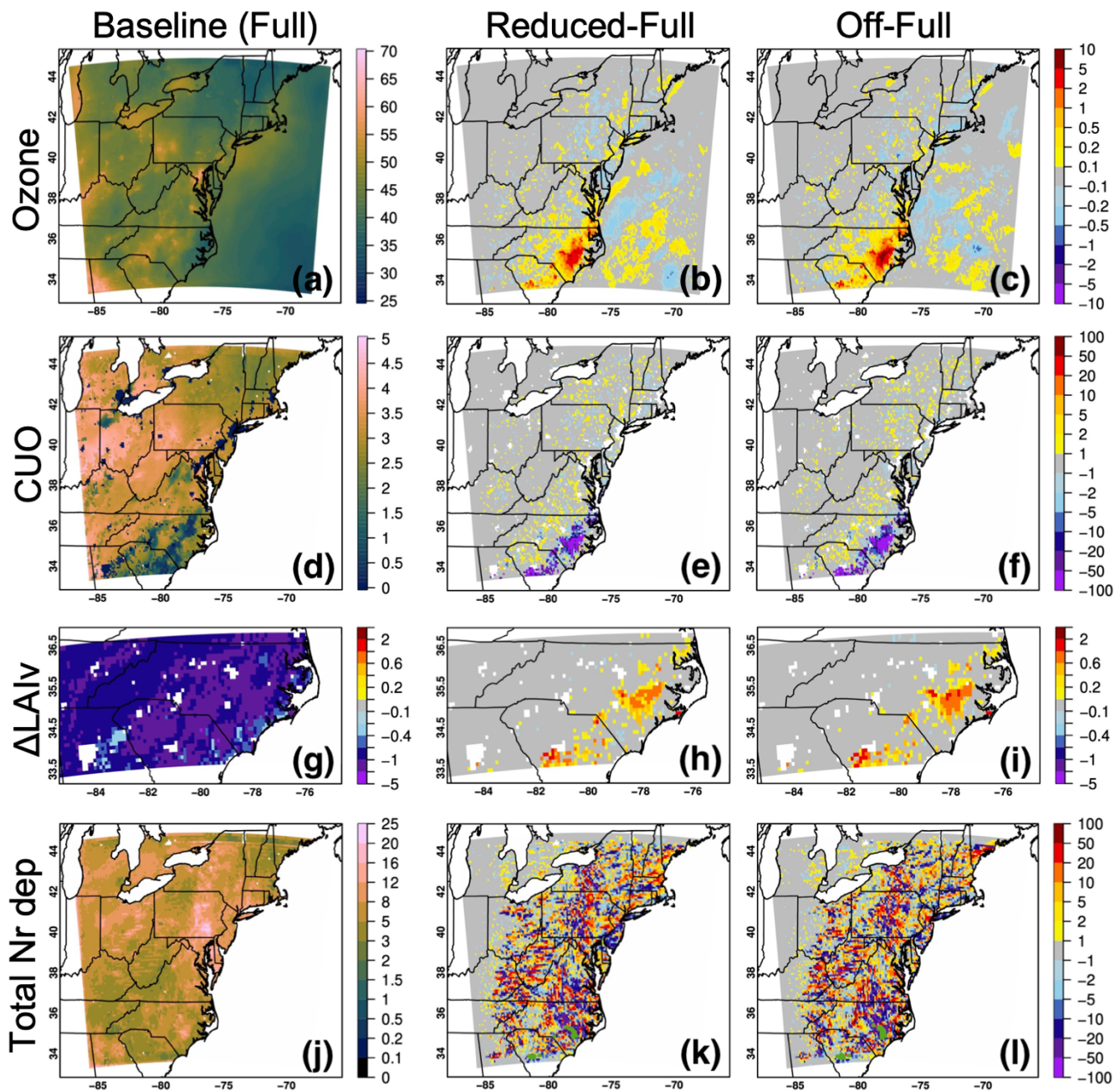


Figure 14: July 2022-July 2018 monthly differences in (a–c) SSM ($\text{m}^3 \text{m}^{-3}$) indicated by bias-corrected SMAP, free-running and SMAP-constrained WRF-Chem initial conditions (ICs); (d–f) early afternoon NO₂ columns (%) based on TROPOMI, free-running and SMAP-constrained WRF-Chem results; (g–i) daytime surface O₃ concentrations (ppbv) based on AQS observations, free-running and SMAP-constrained WRF-Chem results; and (j–l) daytime surface air temperature (K) based on the National Centers for Environmental Prediction (NCEP) Surface Observational Weather Data product, free-running and SMAP-constrained WRF-Chem results. Green circles highlight areas in/around Virginia where improvements in WRF-Chem land ICs notably improved the weather, NO₂ and O₃ fields. Additional information on the SMAP data assimilation (DA) impacts is included in Fig. S18.

1320



1325

Figure 15: (a) Daytime surface O₃ concentration (ppbv, with the RMSE relative to AQS data of ~5.6 ppbv); (d) period-cumulated O₃ stomatal uptake (mmol m⁻²); (g) O₃ impacts on leaf biomass (%) over irrigated areas in/around the Carolinas; and (h) total Nr deposition overland (kgN ha⁻¹ a⁻¹) from the baseline simulation during 21–30 June 2022, and (b;c;e;f;h;i;k;l) their sensitivities to adjustments in irrigation schemes. Sensitivity results are in ppbv for surface O₃ concentration, and in % for all other plots. Green areas in (k;l) marked the grids where Student's *t*-tests comparing Nr deposition from the baseline and sensitivity simulations gave smaller-than-0.05 *p* values.

1330

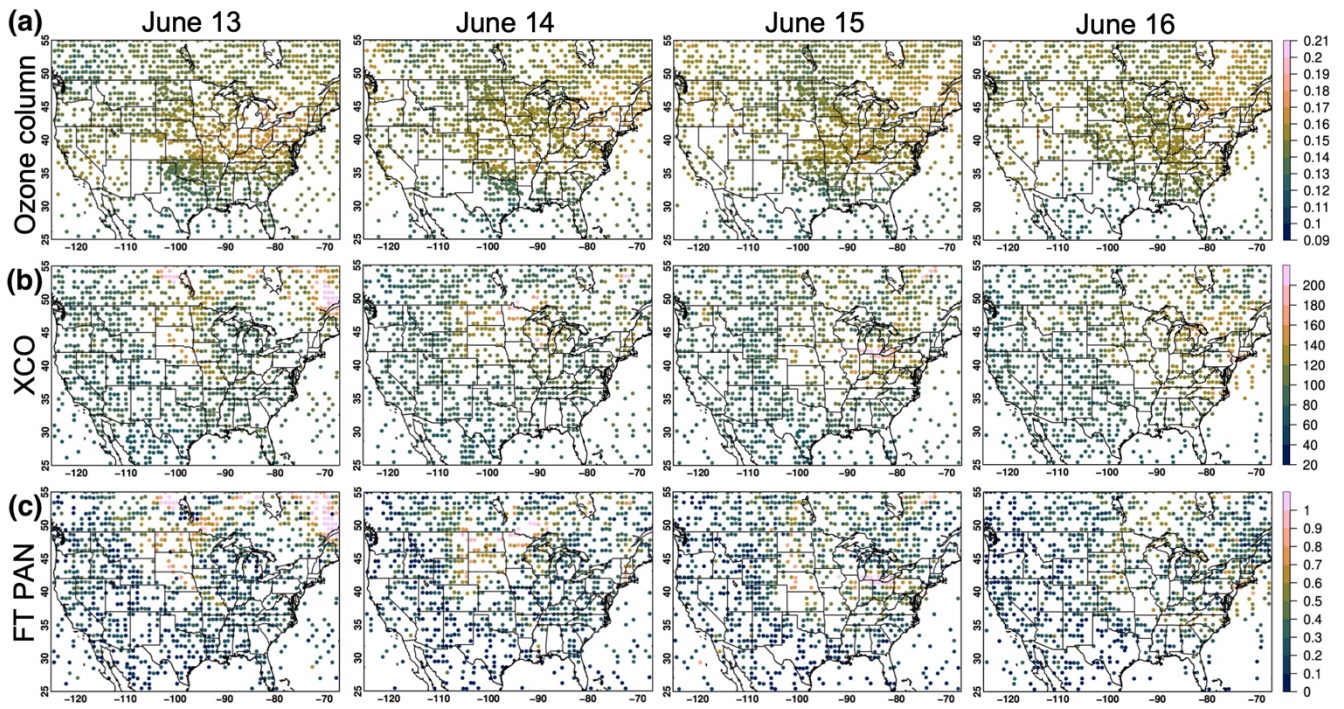


Figure 16: JPSS-1/CrIS observed (a) O_3 columns (mol m^{-2}); (b) column-averaged CO mixing ratios (ppbv); and (c) column-averaged PAN mixing ratios (ppbv) for the free troposphere between 825 and 215 hPa, during 13–16 June 2023.

1335

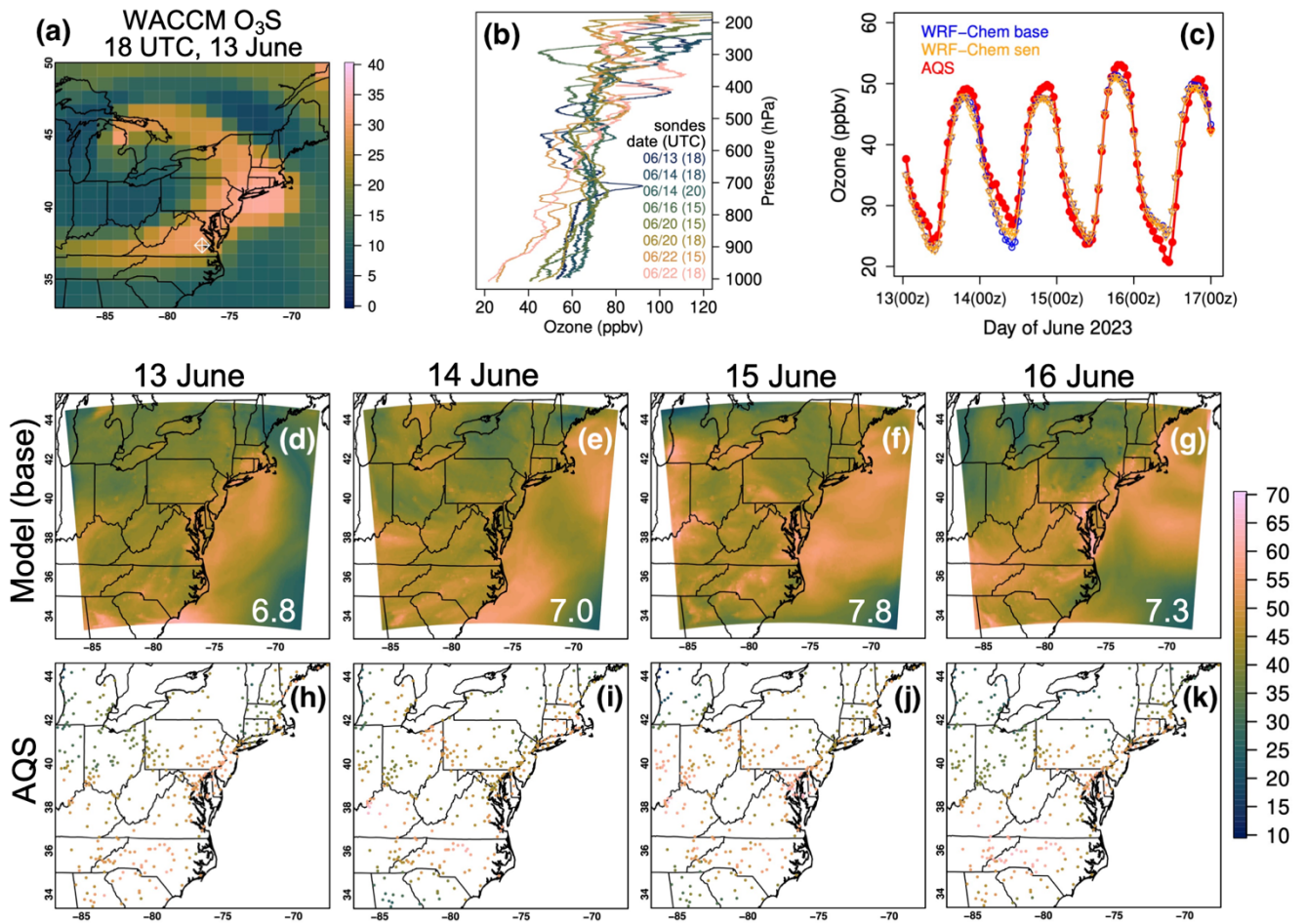
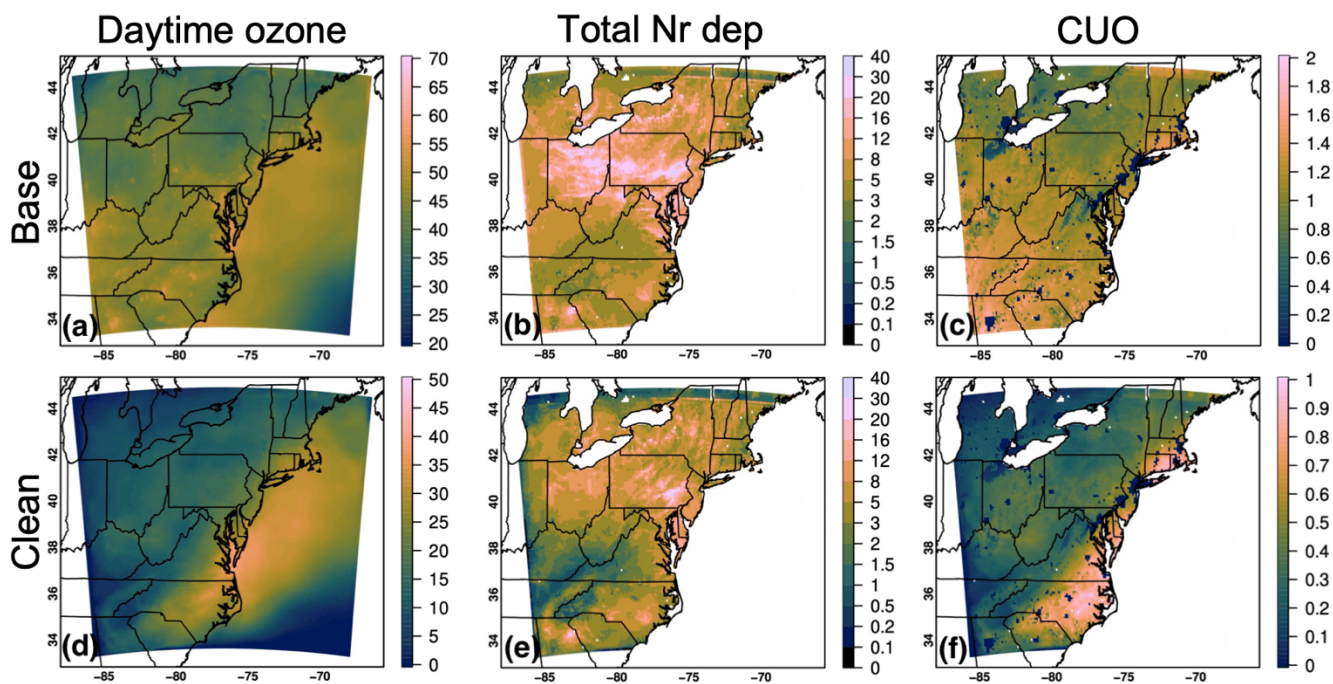


Figure 17: (a) WACCM model stratospheric O₃ tracer (ppbv) results at ~700h Pa at 18 UTC of 13 June 2023, with location of the RRC site being indicated by a white diamond; (b) Ozonesonde profiles launched from the RRC; (c) Timeseries of the domain-mean observed and WRF-Chem modeled hourly surface O₃ during 13–16 June 2023 at AQS sites; and daytime surface O₃ concentrations (ppbv) on 13–16 June 2023 from (d–g) the WRF-Chem baseline simulation and (h–k) AQS sites. WRF-Chem vs. AQS RMSEs (ppbv) are indicated in the lower-right corners of (d–g).

1340



1345 **Figure 18:** (a;d) Daytime surface O₃ concentrations (ppbv); (b;e) total Nr deposition overland (kgN ha⁻¹ a⁻¹); and (c;f) period-cumulated O₃ stomatal uptake (mmol m⁻²) during 13–16 June 2023 from the (a–c) baseline simulation and (d–f) sensitivity simulation with clean chemical BCs.